The Astrophysical Journal, 1010:86 (20pp), 2026 October 10 https://doi.org/10.3847/1538-4357/aea07b
© 2026. The Author(s). Published by the American Astronomical Society.
OPEN ACCESS

# Direct Pathway to the Early Supermassive Black Holes: A Red Super-Eddington Quasar in a Massive Starburst Host at $z = 7.2$

Qinyue Fei[1], Seiji Fujimoto[1], Gabriel Brammer[2], Ruancun Li[3], Luis C. Ho[4,5], Volker Bromm[6,7,8], Javier Álvarez-Márquez[9], Yoshihisa Asada[1], Guillermo Barro[10], Luis Colina[9], Pratika Dayal[1,11,12], Steven L. Finkelstein[6,8], Johan P. U. Fynbo[2], Michele Ginolfi[13,14], Kohei Inayoshi[4], Vasily Kokorev[6,8], Gene C. K. Leung[6,15], Jorryt Matthee[16], Romain A. Meyer[17], Rohan P. Naidu[18,27], Masafusa Onoue[4,19,20,21], Pablo G. Pérez-González[9], Charles L. Steinhardt[22], Francesco Valentino[2,23], Fabian Walter[24,25,26], Mengyuan Xiao[17], and Haowen Zhang[11]

[1] Dunlap Institute for Astronomy & Astrophysics, University of Toronto, 50 St. George Street, Toronto, Ontario, M5S 3H4, Canada; qyfei.astro@gmail.com
[2] Cosmic Dawn Center (DAWN), Niels Bohr Institute, University of Copenhagen, Jagtvej 128, København N, DK-2200, Denmark
[3] Max-Planck-Institut für extraterrestrische Physik, Gießenbachstraße 1, 85748, Garching bei München, Germany
[4] Kavli Institute for Astronomy and Astrophysics, Peking University, Beijing 100871, People's Republic of China
[5] Department of Astronomy, School of Physics, Peking University, Beijing 100871, People's Republic of China
[6] Department of Astronomy, The University of Texas at Austin, Austin, TX 78712, USA
[7] Weinberg Institute for Theoretical Physics, The University of Texas at Austin, Austin, TX 78712, USA
[8] Cosmic Frontier Center, The University of Texas at Austin, Austin, TX 78712, USA
[9] Centro de Astrobiología (CAB), CSIC-INTA, Ctra. de Ajalvir km 4, Torrejón de Ardoz, E-28850, Madrid, Spain
[10] University of the Pacific, Stockton, CA 90340, USA
[11] Canadian Institute for Theoretical Astrophysics, 60 St. George Street, University of Toronto, Toronto, ON M5S 3H8, Canada
[12] Department of Physics, University of Toronto, 60 St. George Street, Toronto, ON M5S 3H8, Canada
[13] Università di Firenze, Dipartimento di Fisica e Astronomia, via G. Sansone 1, 50019, Sesto Fiorentino, Florence, Italy
[14] INAF—Arcetri Astrophysical Observatory, Largo E. Fermi 5, I-50125, Florence, Italy
[15] MIT Kavli Institute for Astrophysics and Space Research, 77 Massachusetts Avenue, Cambridge, MA 02139, USA
[16] Institute of Science and Technology Austria (ISTA), Am Campus 1, 3400 Klosterneuburg, Austria
[17] Department of Astronomy, University of Geneva, Chemin Pegasi 51, 1290 Versoix, Switzerland
[18] MIT Kavli Institute for Astrophysics and Space Research, 70 Vassar Street, Cambridge, MA 02139, USA
[19] Waseda Institute for Advanced Study (WIAS), Waseda University, 1-21-1, Nishi-Waseda, Shinjuku, Tokyo 169-0051, Japan
[20] Kavli Institute for the Physics and Mathematics of the Universe (WPI), Institutes for Advanced Study, The University of Tokyo, Kashiwa, Chiba 277-8583, Japan
[21] Center for Data-Driven Discovery, Kavli IPMU (WPI), UTIAS, The University of Tokyo, Kashiwa, Chiba 277-8583, Japan
[22] Department of Physics and Astronomy, University of Missouri, 701 S. College Avenue, Columbia, MO 65201, USA
[23] DTU Space, Technical University of Denmark, Elektrovej 327, DK2800 Kgs. Lyngby, Denmark
[24] Max Planck Institut für Astronomie, Königstuhl 17, D-69117 Heidelberg, Germany
[25] California Institute of Technology, Pasadena, CA 91125, USA
[26] National Radio Astronomy Observatory, Pete V. Domenici Array Science Center, P.O. Box O, Socorro, NM 87801, USA
*Received 2026 February 7; revised 2026 August 11; accepted 2026 August 14; published 2026 October 9*

## Abstract

We present a panchromatic optical-millimeter characterization of GNz7q, a recently identified X-ray-weak, rapidly growing red quasar embedded within a dusty starburst galaxy at $z = 7.1899$, using the full suite of JWST/NIRCam, NIRSpec, Mid-Infrared Instrument (MIRI), and archival NOEMA observations. Our deep NIRSpec/G395M spectroscopy reveals unambiguous broad Balmer emission (FWHM $= 2221 \pm 20$ km s$^{-1}$), confirming a super-Eddington accreting black hole (BH) ($\lambda_{\rm Edd} = 2.7 \pm 0.4$) with a mass of $\log(M_{\rm BH}/M_\odot) = 7.55 \pm 0.34$, using accretion-rate-corrected BH mass estimators. After subtracting the point source, we robustly detect stellar emission from the host galaxy across multiple NIRCam and MIRI filters. Our joint morphological-spectral analysis yields a stellar mass of $\log(M_*/M_\odot) = 10.5 \pm 0.4$ and an intense star formation rate of SFR $= 330 \pm 97\,M_\odot\,{\rm yr}^{-1}$, confirming the host as a massive, dusty starburst galaxy. We find that GNz7q lies on the local $M_{\rm BH}$–$M_*$ relation ($M_{\rm BH}/M_* \simeq 0.001$) and is well positioned to evolve into the locus of massive Sloan Digital Sky Survey (SDSS) quasars with $\log(M_{\rm BH}/M_\odot) \approx 9$ and $M_* \approx 10^{11}\,M_\odot$ at $z \sim 6$, owing to its remarkably rapid growth in both the BH and its host galaxy. This stands in stark contrast to many recently reported JWST active galactic nucleus populations at similar redshifts, including the little red dots, whose weak or undetected star formation makes it difficult for them to grow into the massive galaxies hosting SDSS-like quasars. These results suggest that GNz7q marks a rare, pivotal phase of early BH–galaxy coevolution, plausibly providing a crucial direct pathway to the supermassive BH systems within the first billion years of the Universe.

*Unified Astronomy Thesaurus concepts:* AGN host galaxies (2017); Quasars (1319); Active galactic nuclei (16); Supermassive black holes (1663); High-redshift galaxies (734)

## 1. Introduction

The discovery of luminous quasars at redshift $z \gtrsim 6$ has fundamentally challenged our understanding of the early Universe (e.g., A. Smith & V. Bromm 2019; T. E. Woods et al. 2019). The existence of supermassive black holes

[27] Hubble Fellow.

Original content from this work may be used under the terms of the Creative Commons Attribution 4.0 licence. Any further distribution of this work must maintain attribution to the author(s) and the title of the work, journal citation and DOI.

(SMBHs) with masses exceeding $10^9\,M_\odot$ less than 1 Gyr after the Big Bang (e.g., X. Fan et al. 2001, 2006; D. J. Mortlock et al. 2011; E. Bañados et al. 2018; F. Wang et al. 2021a) necessitates specific mechanisms for rapid BH growth. Theoretical models suggest that these giants grew from either heavy seeds, arising from the direct collapse of massive primordial gas clouds, or light seeds originating in stellar remnants that underwent continuous, super-Eddington accretion (e.g., M. Volonteri 2012; K. Inayoshi et al. 2020). In addition, these high-$z$ quasars appear to host "overmassive" BHs (M. A. Stone et al. 2024; M. Yue et al. 2024; R. Li et al. 2026), relative to the stellar mass of their host galaxies when compared to the local $M_{\rm BH}$–$M_*$ relations (J. Kormendy & L. C. Ho 2013; A. E. Reines & M. Volonteri 2015; J. E. Greene et al. 2020; M.-Y. Zhuang & L. C. Ho 2023).

The launch of JWST has opened a new window into this field, unveiling a previously hidden population of fainter active galactic nuclei (AGNs) at high redshifts (e.g., Y. Harikane et al. 2023; D. D. Kocevski et al. 2023; V. Kokorev et al. 2023; R. L. Larson et al. 2023; L. J. Furtak et al. 2024; R. Maiolino et al. 2024a, 2024b; J. Matthee et al. 2024; X. Lin et al. 2024, 2026; A. J. Taylor et al. 2025a, 2025b; R. E. Hviding et al. 2025; Q. Fei et al. 2026). Identified by broad rest-frame optical Balmer lines, these sources enable the study of lower-mass BHs ($M_{\rm BH} \sim 10^5$–$10^8\,M_\odot$) in the early Universe. In contrast to massive, luminous quasars that display mature features (S. E. I. Bosman et al. 2024; S. E. I. Bosman et al. 2025), these objects likely represent a nascent phase of BH growth (K. Inayoshi 2025; J. Jeon et al. 2025).

Many of these lower-luminosity AGNs reside in low-mass galaxies ($\sim 10^8\,M_\odot$), revealing BH-to-stellar mass ratios ($M_{\rm BH}/M_*$) that deviate more dramatically from the local relationship, with some objects exhibiting values 10 to 100 times higher than the local benchmark (e.g., T. Izumi et al. 2019; R. Maiolino et al. 2024a; C.-H. Chen et al. 2025b; J. Li et al. 2025), though this deviation may be less extreme if BH masses are systematically lower by $\sim$1 dex as recently suggested (e.g., J. E. Greene et al. 2026; H. Umeda et al. 2026; Y. Asada et al. 2026). In addition, several recent numerical simulations and theoretical models further suggest that traditional virial mass estimators may be subject to significant systematic biases when applied to super-Eddington accreting BHs, necessitating the use of accretion-rate-dependent corrections (e.g., A. King 2024; A. Lupi et al. 2024; A. Trinca et al. 2026b). The presence of such high $M_{\rm BH}/M_*$ ratios may directly support the existence of "heavy seeds" formed via direct collapse BHs, providing a possible mechanism for the rapid early growth of SMBHs (R. Maiolino et al. 2024a; F. Pacucci & A. Loeb 2024; J. Jeon et al. 2026), or implicate more exotic formation channels (e.g., the core collapse of self-interacting dark matter; F. Jiang et al. 2026) or even primordial BHs (e.g., R. Bean & J. Magueijo 2002; B. Carr & F. Kühnel 2020; P. Dayal 2024; S. Zhang et al. 2025). However, we need to consider that this observed deviation could be partially driven by observational biases, since flux-limited surveys may preferentially detect systems where the central engine outshines the host, artificially skewing samples toward high-mass ratios (J. Li et al. 2025; J. Silverman et al. 2025).

Crucially, whether these faint, overmassive sources represent the direct progenitors of the luminous quasars observed at $z \sim 6$ remains an open question. To fully bridge these populations, it is essential to investigate the coevolution of both the BH and the host galaxy, yet significant physical discrepancies exist between the two regimes. Unlike the vigorous starbursts associated with luminous quasar host galaxies (e.g., F. Walter et al. 2004; R. Wang et al. 2010, 2013; R. Decarli et al. 2018; B. P. Venemans et al. 2020; M. Neeleman et al. 2021; Q. Fei et al. 2025), JWST-discovered AGNs often exhibit generally low star formation activity, characterized by strong upper limits on their rest-frame IR-derived star formation rates (SFRs; H. B. Akins et al. 2025; C. M. Casey et al. 2025). Furthermore, these sources usually display low Eddington ratios ($\lambda_{\rm Edd} \approx 0.1$; Y. Harikane et al. 2023; R. Maiolino et al. 2024b), contrasting with the rapid accretion required to build SMBHs.

This ambiguity is further compounded by systematic uncertainties in deriving BH properties at these epochs. Standard estimators rely on empirical scaling relations calibrated in the local Universe, which may be inapplicable to high-$z$ faint AGNs given their distinct spectral characteristics,[28] such as deviant broad emission-line profiles (V. Kokorev et al. 2026; V. Rusakov et al. 2026) and complex absorption features (F. D'Eugenio et al. 2025; B. Wang et al. 2025). Theoretical frameworks describing these systems introduce additional complexity (S.-J. Chang et al. 2025; K. Inayoshi & R. Maiolino 2025; R. P. Naidu et al. 2026); these model dependencies imply uncertainties in BH mass and accretion rates ($\dot{\mathcal{M}}$) of up to $\sim$1 dex (J. E. Greene et al. 2026). Consequently, to bridge this gap and empirically verify the transition from faint seeds to luminous giants, it is crucial to investigate rare "transitional" sources (S. Fu et al. 2026), which occupy the intermediate parameter space and offer simultaneous, robust constraints on both the central AGN and the host galaxy. Comparable systematic uncertainties affect the measurement of the host galaxies. The decomposition of the host galaxy is inherently degenerate due to the overwhelming AGN continuum and limitations in point-spread function (PSF) subtraction (M. Mechtley et al. 2012; M. A. Marshall et al. 2020). Furthermore, these photometric ambiguities introduce significant scatter in the physical properties derived via spectral energy distribution (SED) fitting (X. Ding et al. 2023, 2025).

In addition to these systematic uncertainties in the measurements, the characterization of the high-redshift AGNs is currently limited by the survey volume of JWST. While the unprecedented sensitivity of JWST has revolutionized our ability to probe faint, low-mass galaxies ($M_* \lesssim 10^9\,M_\odot$) and low-luminosity AGNs into the epoch of reionization, the relatively small field of view of deep surveys (compared to all-sky surveys, such as the Sloan Digital Sky Survey (SDSS); D. J. Eisenstein et al. 2025; M. J. Rieke et al. 2023; H. Atek et al. 2025) restricts the comoving volume sampled. Consequently, the discovery rate of intrinsically rare, massive galaxies ($M_* > 10^{10}\,M_\odot$) embedded within the massive dark matter halos ($M_{\rm DM} \gtrsim 10^{12}\,M_\odot$) at $z > 6$ remains low (A. de Graaff et al. 2025a). This volume limitation results in a paucity of spectroscopically confirmed massive host galaxies harboring accreting massive BHs, leaving the properties of these systems largely unexplored.

In this work, we present deep and comprehensive follow-up observations of a unique red quasar, GNz7q, from JWST

[28] Direct BH mass measurements via resolved JWST integral-field kinematics can provide crucial cross-calibration and validation (I. Juodžbalis et al. 2026).

NIRCam and Mid-Infrared Instrument (MIRI) imaging to NIRSpec G140M+G395M, MIRI Low-Resolution Spectrometer (LRS) and Medium Resolution Spectrograph (MRS) spectroscopy. Originally identified in the GOODS-North field (S. Fujimoto et al. 2022), the source has been spectroscopically confirmed at $z = 7.1899$ via Hubble Space Telescope grism spectroscopy and the detection of [C II] emission with NOEMA. The broadband SED, constrained by NOEMA dust continuum measurements, indicates that the quasar resides within a vigorous starburst host. Notably, the robust mid-infrared (MIR) detection in Spitzer IRAC and MIPS bands confirms that GNz7q satisfies the canonical photometric selection criteria for red quasars (e.g., J. L. Donley et al. 2012). Furthermore, the nondetection in the deep (∼2 Ms) Chandra X-ray observations implies high column densities, consistent with a Compton-thick, highly accreting system. These properties suggest that GNz7q likely represents a pivotal transition phase from a dusty starburst to an optically luminous quasar (e.g., D. B. Sanders et al. 1988; P. F. Hopkins et al. 2008), and might evolve into a luminous quasar at $z \sim 6$.

This paper is organized as follows. In Section 2, we present the observations and data reduction procedures. Section 3 describes the methodology used for the model fitting and spectral analysis. In Section 4, we present the derived physical properties of both the AGN and the host galaxy. Finally, we summarize our conclusions in Section 5. Throughout this paper, we assume a flat universe with $\Omega_m = 0.3$, $\Omega_\Lambda = 0.7$, and $H_0 = 70\,\mathrm{km\,s^{-1}\,Mpc^{-1}}$. We use magnitudes in the AB system (J. B. Oke & J. E. Gunn 1983).

## 2. Data

### 2.1. NIRCam Image

The NIRCam imaging data are retrieved from two programs: GO-4762 (PIs: S. Fujimoto & G. Brammer) and the FRESCO survey (GO-1895; P. A. Oesch et al. 2023). The source was observed with NIRCam F090W, F115W, F182M, F210M, F356W, and F444W filters. The detailed data reduction procedures are consistent with the standard data reduction procedure (e.g., D. J. Eisenstein et al. 2025; P. A. Oesch et al. 2023; H. Atek et al. 2025). Here we briefly mention the process.

The reduction of NIRCam imaging data commenced with the processing of uncalibrated files using the JWST Science Calibration Pipeline (v12.0.9) and the Calibration Reference Data System (CRDS) context file `jwst_1321.pmap`. Beyond standard STScI procedures, we implemented custom steps to mitigate artifacts, including the removal of snowballs, wisps, cosmic rays, persistence, and diffraction spikes, alongside an initial $1/f$ noise correction. Following Stage 2 pipeline processing, we applied a secondary correction for residual $1/f$ noise via sigma-clipping and performed two-dimensional background subtraction using the `sep` package. The data were then co-added through Stage 3 to produce final astrometrically aligned mosaics (referenced to Gaia stars) with pixel scales of 20 mas pix$^{-1}$ for short-wavelength bands and 40 mas pix$^{-1}$ for long-wavelength bands. The NIRCam grism spectrum also confirms the presence of the broad component (P. A. Oesch et al. 2023). We prioritize the NIRSpec data for our quantitative analysis due to its higher signal-to-noise ratio (SNR).

### 2.2. MIRI Image

The MIRI imaging data are also retrieved from two programs: F1280W from GO-4762 (PIs: S. Fujimoto & G. Brammer) and F1000W and F2100W from the MEOW survey (GO-5407; G. C. K. Leung et al. 2024). The F1280W data were reduced following the standard procedures established by the Dawn JWST Archive (F. Valentino et al. 2023) and widely used in public surveys (e.g., PRIMER J. S. Dunlop et al. 2021). Specifically, we retrieved the Level-2 products and processed them using the `grizli` software package (G. Brammer & J. Matharu 2021; G. Brammer et al. 2022), adopting the methodology described in detail by F. Valentino et al. (2023).

For F1000W and F2100W, the data publicly available in September 2025 for the GOODS-N field, jointly with the proprietary MEOW data, were reduced with the JWST Rainbow pipeline following the methodology described in P. G. Pérez-González et al. (2024). The observations come from PIDs 1181, 1264, 2926, 4762, and 5407, and mosaics were constructed for filters F560W, F770W, F1000W, F1280W, F1800W, and F2100W. The position of GNz7q is only covered at 10, 12.8, and 21 $\mu$m. Details about this reduction (jointly with a similar effort in other fields such as GOODS-S, the Extended Groth Strip, or COSMOS) will be presented in P. G. Pérez-González et al. (2026, in preparation). We briefly describe here the methodology. The JWST Rainbow database uses the official JWST pipeline, adding some extra bespoke reduction steps to deal with the background homogenization of the MIRI images. For this paper, the reduction was carried out with JWST version v1.19.41 reference files in `jwst_1413.pmap`. A key component of this workflow is the "superbackground" strategy, in which background maps for individual exposures are constructed using the full set of campaign images, with known sources masked to mitigate bias. This approach yields a highly homogeneous background in terms of both level and noise. Quantitatively, this method reduces the standard deviation of background pixels in individual `cal.fits` files by a factor of ∼3.5 relative to the standard pipeline, resulting in a sensitivity improvement of 0.8 mag in the final mosaic. (See Appendix A in P. G. Pérez-González et al. 2024 for further details; see also G. Östlin et al. 2025 and S. Alberts et al. 2024 reporting similar improvements in the noise of the final mosaics.)

### 2.3. NIRSpec Data

The deep spectroscopic follow-up of GNz7q was obtained with JWST/NIRSpec as part of the program (PID 4762 l PIs: S. Fujimoto & G. Brammer), using the Multi-Object Spectroscopy mode with the G395M grating in the F290LP filter ($R \sim 1000$) and the G140M grating in the F140LP filter. We design the NIRSpec micro-shutter assembly (MSA) configurations following a strategy similar to that adopted in the UNCOVER survey (R. Bezanson et al. 2024; S. H. Price et al. 2025), aiming both to secure the full integration on GNz7q and to maximize the multiplexing return of the deep G395M observations. To this end, we implement a two-tiered prioritization scheme distinguishing between (1) extraordinary or otherwise scientifically unique individual sources, and (2) samples of galaxies of broader interest (e.g., statistical sets of $z > 4$ galaxies). Within this framework, the ranking order is set such that high-priority individual sources are placed first,

followed by interesting but less extraordinary individual galaxies, and finally sample-based sources with equal priority within a given catalog. This scheme is used in combination with our custom MSA optimization algorithm to maximize slit allocation efficiency. As a result, a total of 241 sources are allocated slits. The on-source integration time for those sources is 7525 s ($\simeq$2.1 hr). The data were reduced with the `msaexp` pipeline (G. Brammer 2023) following standard procedures (e.g., A. de Graaff et al. 2025b; K. E. Heintz et al. 2025; R. P. Naidu et al. 2026; F. Valentino et al. 2025).

### 2.4. MIRI MRS and LRS

GNz7q was observed with the MRS (M. Wells et al. 2015; I. Argyriou et al. 2023) of the MIRI (G. H. Rieke et al. 2015; G. S. Wright et al. 2015, 2023) on GNz7q as part of the Cycle 3 JWST program GO-4762 (PIs: S. Fujimoto & G. Brammer). The observations were performed with the MRS medium band that covers the wavelength ranges of 5.66−6.63 $\mu$m, 8.67−10.13 $\mu$m, 13.34−15.57 $\mu$m, and 20.69−24.48 $\mu$m for Channels 1, 2, 3, and 4, respectively. We focus on Channel 3 that covers the Paschen-$\alpha$ (Pa$\alpha$) emission line at a redshift of 7.2. The total on-source integration time corresponds to 11,939 s (3.3 hr), distributed in 8 dither positions that combine the positive and negative dither patterns optimized for point-like sources. For each dither position, a total of two integrations with 17 groups each were obtained using the SLOWR1 readout mode.

The MRS observations were processed with version 1.17.1 of the JWST calibration pipeline and context 1322 of the CRDS. We followed the standard MRS pipeline procedure (H. Bushouse et al. 2024), with additional customized steps to improve the quality of the final MRS calibrated products (see J. Álvarez-Márquez et al. 2023, 2024 for details). The final Channel 3 cube has a spatial and spectral sampling of $0\farcs2 \times 0\farcs2 \times 2.5$ nm (D. R. Law et al. 2023), respectively, and a resolving power of about 2500 (A. Labiano et al. 2021; O. C. Jones et al. 2023).

We extracted the 1D integrated spectra of GNz7q using a circular aperture with a radius equal to $0\farcs5$ for Channel 3 (see Figure 4). We also extracted 15 1D background spectra using the same apertures at random positions of the MRS' field of view, clean of any emission from the source. We combined these spectra to generate the 1D median and standard deviation of the local background for Channel 3. The median, which is compatible with zero, was subtracted from the GNz7q spectra with the goal of removing any systematic residual feature left in the MRS calibration process. The standard deviation was assumed to be the 1 $\sigma$ uncertainty of GNz7q spectra. As GNz7q is considered spatially unresolved in the MRS observations, we implemented an aperture correction to derive the total Pa$\alpha$ spectrum of GNz7q. For the selected apertures in Channel 3, the aperture correction factor is 1.59 following the MRS PSF (I. Argyriou et al. 2023).

Data reduction and calibration for the MIRI LRS observations are conducted utilizing the standard JWST pipeline in conjunction with the `msaexp` (G. Brammer 2023). One-dimensional spectral extraction was performed via the optimal extraction method (K. Horne 1986), employing a point-source profile derived from calibration observations of the A1V standard star BD+601753 (Program ID: CAL-6620; G. Sloan et al. 2024). The 2D spectrum and the extracted 1D spectrum are presented in Figure B1, and the data analysis is presented in Section 3.3.

## 3. Analysis

### 3.1. NIRSpec G395M Spectrum and Fitting

We perform the spectral decomposition using `GalfitS` (C.-H. Chen et al. 2025b, 2025a; R. Li et al. 2026), a software developed for simultaneous SED, morphological, and spectral analysis, which can also be used to fit the spectra. The spectral fitting methodology implemented in `GalfitS` is similar to that of established AGN analysis software (e.g., `pyQSOFIT`, `fantasy`; H. Guo et al. 2018; D. Ilić et al. 2020; W. Ren et al. 2024), principally decomposing the data into host galaxy continuum, AGN continuum, and emission-line features. However, given the high luminosity of this source (J. Yang et al. 2023), the observed spectrum is dominated by the central AGN. We therefore consider the stellar continuum contribution negligible in the rest-frame optical and exclude it from the fitting process. This approximation is subsequently confirmed by the broadband SED analysis presented in Section 4.3 (see also Figure 7). Although broadband SED fitting indicates a significant host galaxy contribution within the MIRI filters, its impact in the rest-frame optical remains subdominant and is comparable to the local noise floor. To verify this, we performed a spectral decomposition using `pyQSOFIT`, incorporating both AGN and host components. The results are consistent with our primary analysis, confirming that the host galaxy contribution is negligible across the rest-frame optical regime. Consequently, our final spectral model consists of two primary AGN components: a continuum model (comprising a double power law and an iron pseudo-continuum) and the emission-line models.

The power-law continuum is parameterized by its amplitude ($f_0$), spectral index ($\alpha$), and a pivot wavelength ($\lambda_0$) fixed at 5000 Å in the rest frame ($f_\lambda = f_0(\lambda/\lambda_0)^{-\alpha}$). For the iron pseudo-continuum, we employ the empirical Fe II template derived from I Zw 1 (T. A. Boroson & R. F. Green 1992). The free parameters for this component are amplitude, velocity shift, and broadening velocity width.

The emission-line model incorporates the permitted emission lines (H$\alpha$, H$\beta$, H$\gamma$, and He II) and the forbidden lines ([O III] $\lambda\lambda$4959, 5007 and [N II] $\lambda\lambda$6548, 6584), assuming a tied line width across all species. We model the [O III] lines using two distinct components: a primary narrow-core component tracing the systemic velocity, and a secondary, broader, blueshifted component to account for potential gas outflows. During the fit, the flux ratio of the [O III] $\lambda$5007 to $\lambda$4959 doublet components is held fixed at its theoretical value of 2.98 (P. J. Storey & C. J. Zeippen 2000). The line ratio for the [N II] $\lambda\lambda$6548,6584 doublets is also fixed to its theoretical value of 2.94.

The decomposed [O III] profile is then used to impose a set of physical constraints on the other emission lines. The profile of the [O III] lines is adopted as the template for all narrow-line components, i.e., the systemic velocity, the line width, and the line ratio between the core and outflow components are fixed when fitting the other forbidden lines and the narrow component of the Balmer lines. We adopted the [O III] doublet as the narrow-line template, as it is a standard tracer and represents the strongest, least-blended forbidden lines in our spectrum. Although the [S II] doublet is another common

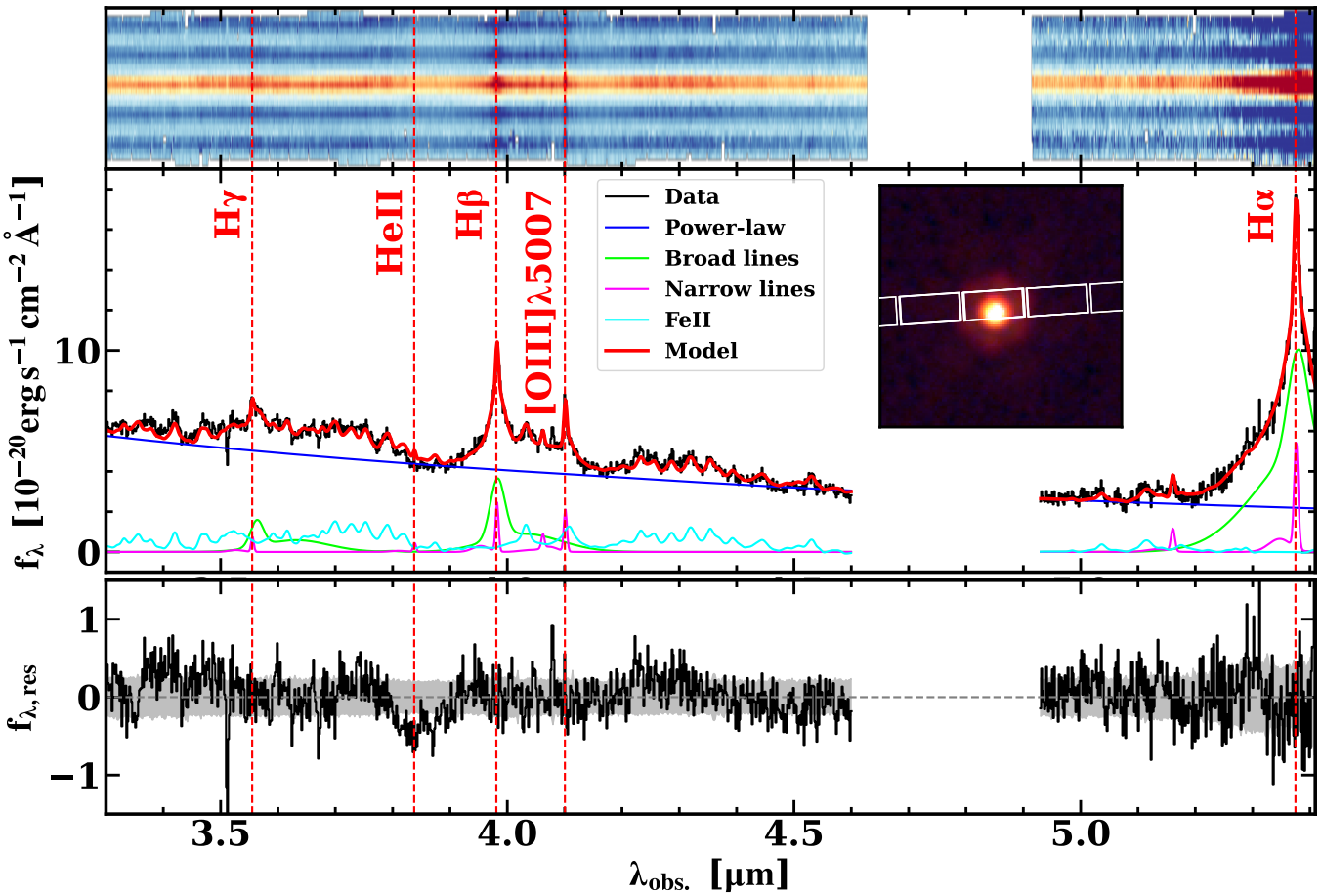



**Figure 1.** The NIRSpec/MSA spectrum and the best-fit model. Top panel: the 2D spectrum generated from the JWST/NIRSpec observation. Middle panel: the 1D spectrum (black line) extracted from the 2D spectrum and the best-fitting result (red line). The best-fit model consists of several components, including a featureless power-law continuum (blue line), an iron pseudo-continuum (cyan line), the narrow component of emission lines (magenta line), and the broad component of Balmer lines (green line). Bottom panel: the residual between the data and the best-fit model (black line), and the uncertainties (gray dashed region).

choice, it falls outside the wavelength coverage of our data and is therefore not used in our fitting. We characterize the broad component of the Balmer lines using two distinct Gaussian components. This double-Gaussian model is necessary to characterize the shape of the spectrum. We will explain it in the next section and discuss the potential origin of the line profile in Section 4.1. To mitigate the degeneracy between the broad Balmer line profiles and the iron pseudo-continuum, the kinematic parameters (i.e., line width and velocity center) of each broad component are tied to be the same across the H$\alpha$, H$\beta$, and H$\gamma$ lines.

Using this model, we perform the fitting using `GalfitS` with the `multi-task` option. This routine executes the fitting algorithm multiple times independently. For each iteration, a new set of initial parameters is randomly sampled from the predefined, physically allowed parameter space. The solution from this ensemble of fits that yields the global minimum reduced chi-squared ($\chi^2_\nu$) is then adopted as our final best fit.

The results of our spectral decomposition are presented in Figure 1. The composite model provides an excellent representation of the observed rest-optical spectrum. All significant spectral features, including the various emission lines and the underlying iron pseudo-continuum, are well reproduced. The quality of the fit is further demonstrated by the residual spectrum (bottom panel in Figure 1), which shows no significant structured features and remains almost entirely within the 1$\sigma$ flux uncertainties.

The best-fit result reveals that the broad Balmer lines can be well-characterized by two components, including a narrower component from the broad-line region (BLR), whose velocity center is consistent with the systemic velocity of the narrow-line region, and a secondary redshifted component (redshifted BLR, dubbed rBLR; $\Delta v \approx 3600\,\mathrm{km\,s^{-1}}$) that has a much broader line width (FWHM $\approx$ 11,000 km s$^{-1}$), which have been observed in quasars at lower redshifts (e.g., J. W. Sulentic et al. 2002; P. Marziani et al. 2009). The origin of this redshifted, extremely broad component is still under debate, including the possibility of inflowing gas feeding the central BH growth or a tidal disruption event (R. Li et al. 2022). We will discuss the reason for this redshifted broad component in a separate paper (S. Fujimoto et al. 2026, in preparation). This two-component structure is required to fit both the H$\beta$ and H$\gamma$ lines (Figure 2), and we further evaluate the necessity of this component in Appendix A. While the same model is applied to H$\alpha$, the constraints on its redshifted component are less clear, as the far red wing extends beyond the spectrum's wavelength coverage.

### 3.2. SED and Morphological Fitting

We perform a simultaneous AGN host galaxy decomposition and SED fitting using `GalfitS` to study the host galaxy

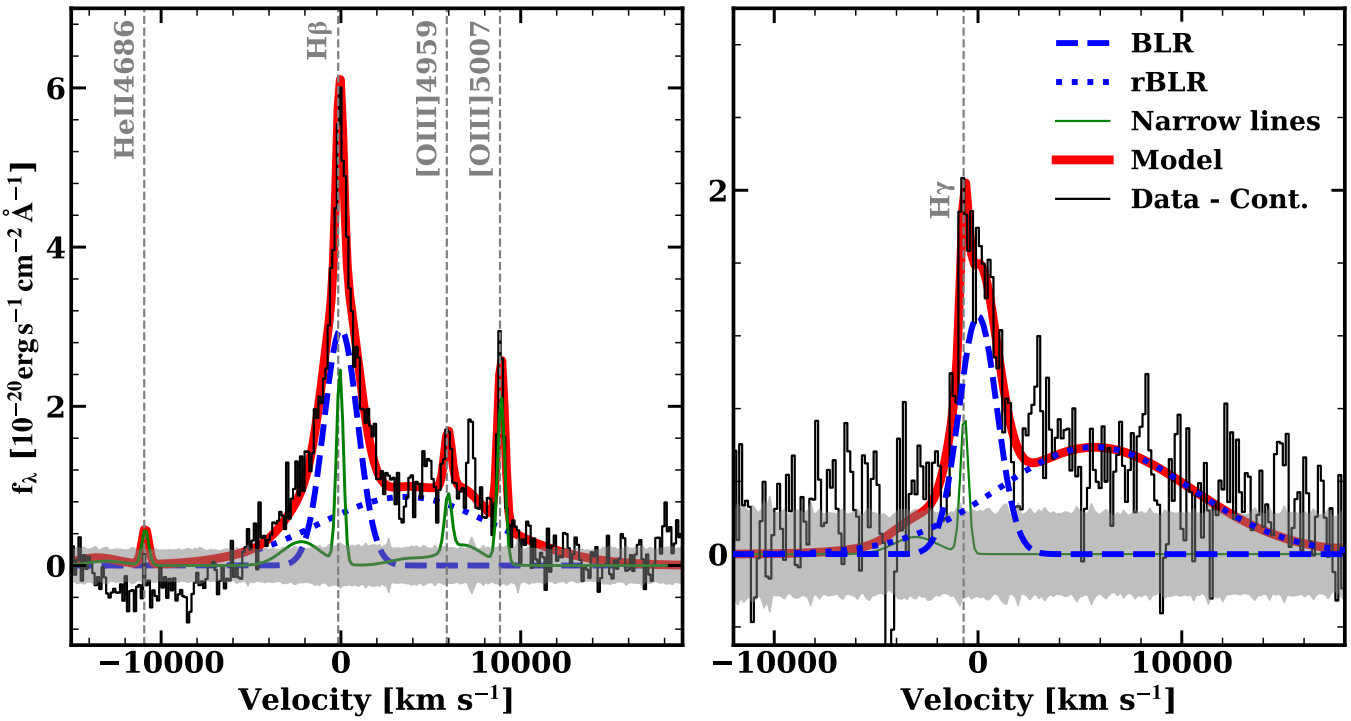



**Figure 2.** Zoom-in view of the H$\beta$ and H$\gamma$ emission lines. The black line shows the observational data after subtracting the global continuum (power law and iron pseudo-continuum). The best-fit model for the emission line is shown in red. Individual components are color coded: narrow emission is shown as the solid green line, and the emission from the BLR is shown as blue dashed lines. The two components for the broad emission line are denoted as the blue dashed and blue dotted (rBLR) lines, respectively. This redshifted component has been observed in some local quasars, in particular, quasars with high Eddington ratio (J. W. Sulentic et al. 2002; P. Marziani et al. 2009).

properties for GNz7q. The software employs a forward modeling approach to simultaneously characterize heterogeneous imaging data, accommodating different instruments, filters, and sensitivities (R. Li et al. 2026, in preparation). The methodology is identical to the procedure established in recent work (R. Li et al. 2026; C.-H. Chen et al. 2025b, 2025a), which already successfully decomposes the AGN and galaxy components for high-$z$ AGNs. As the detailed setup and fitting process are fully described in R. Li et al. (2026), we here provide a brief overview of the setup for reference.

We first construct the empirical PSFs for NIRCam and MIRI images using the field stars (M.-Y. Zhuang & L. C. Ho 2023; R. Li et al. 2026), which give the best description for individual stars compared to the relatively sharper PSF generated from the `WebbPSF` (M. Yue et al. 2024). The empirical PSF is then used for characterizing the unresolved nuclear emission from the quasar. For its nuclear SED, we adopt a nonparametric approach, treating the luminosity in each photometric band as an independent, free parameter.

This PSF is also used for the host galaxy characterization. The host galaxy component is defined by a simultaneous fit to its morphological and SED properties. The morphology is parameterized by a single Sérsic profile, which is defined by its centroid, Sérsic index ($n$), effective radius ($R_e$), axis ratio ($q$), and position angle ($\theta$). The host's stellar SED is modeled via population synthesis assuming a P. Kroupa (2001) initial mass function (IMF). We adopt a nonparametric star formation history (SFH), a choice motivated by the complex, bursty SFHs recently revealed in high-$z$ galaxies by JWST (B. Wang et al. 2024a; L. Wright et al. 2024). The free parameters of this stellar population model include the total stellar mass ($M_*$), the SFR within discrete temporal bins, the stellar metallicity ($Z$), and the $V$-band dust extinction ($A_V$), for which we assume a D. Calzetti et al. (2000) attenuation law. We made a simple assumption of energy balance in which the far-infrared (FIR) energy comes from the stellar light attenuation, and therefore implemented the FIR constraints from the James Clerk Maxwell Telescope and NOEMA observations (S. Fujimoto et al. 2022).

To ensure robust convergence and avoid unphysical solutions, particularly in datasets with limited photometric coverage, the fitting process incorporates several priors. These include constraints from established mass–size relations, mass-dust extinction, and mass–metallicity relations, in addition to an SFH prior (K. Nakajima et al. 2023; G. Maheson et al. 2024; N. Allen et al. 2025).

We perform the fitting process using the nested-sampling algorithm (J. Skilling 2004). We initiated the decomposition by fitting the multiband imaging with only a pure PSF component. This model proved insufficient, as the residual images clearly revealed a significant, extended component spatially offset from the nucleus. Motivated by this, we tested a two-component model comprising a PSF and a Sérsic component, allowing their centers to be fit independently. This model, which converged on the $\sim$2 kpc offset, resulted in a substantially lower BIC, confirming the spatial misalignment between the quasar and this extended host. Finally, we tested a more complex, three-component model to determine if a host component also exists co-spatially with the nucleus. This final model includes a PSF, a Sérsic component co-centered with the PSF, and an offset Sérsic component. This three-component configuration yielded the global minimum BIC, indicating it is the statistically preferred description.

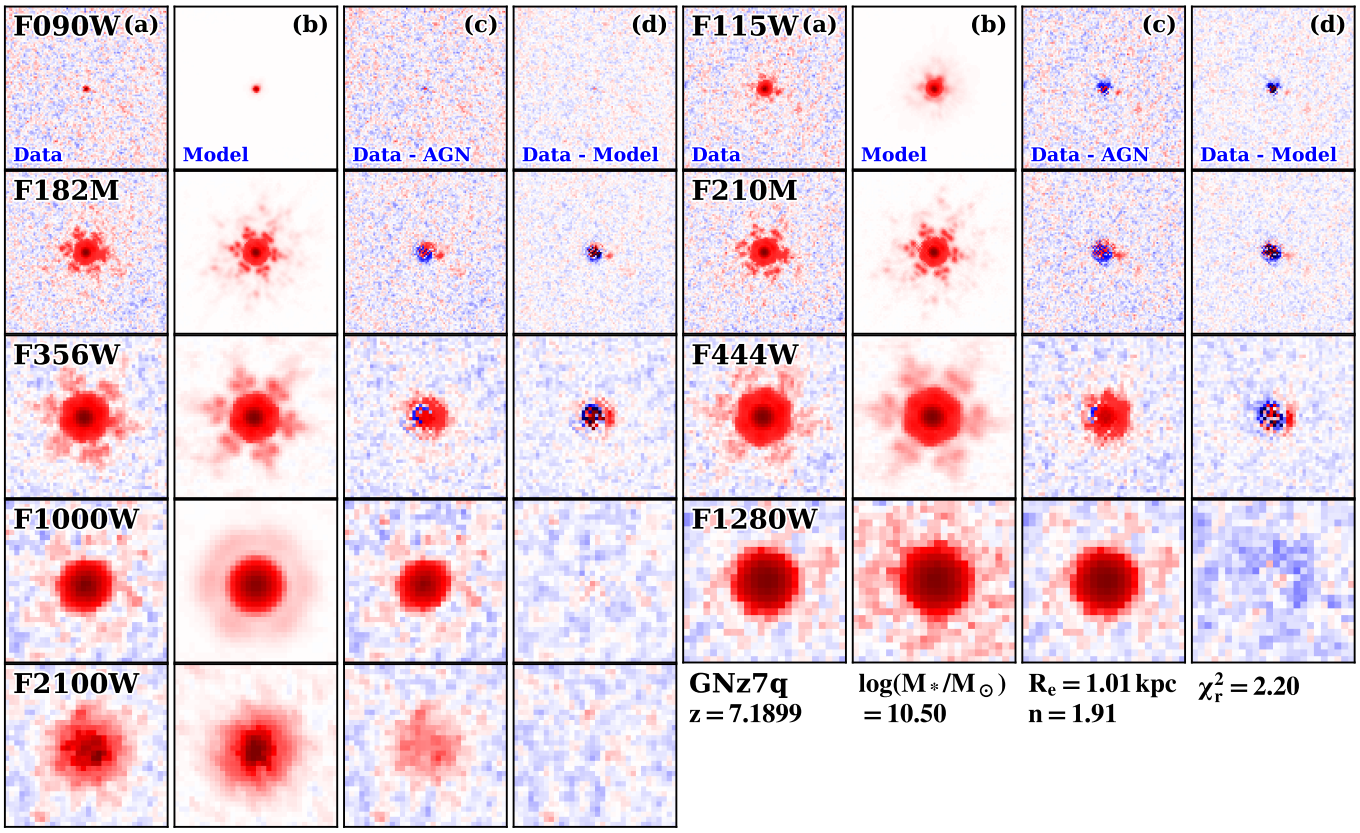



**Figure 3.** Multiband AGN host decomposition for GNz7q. From left to right, the panels display: (a) the original JWST image; (b) the best-fit model; (c) the image of the host galaxy component after PSF subtraction; and (d) the final residual map.

While our primary morphological and spectral analysis utilized `GalfitS`, we employed `cigale` (M. Boquien et al. 2019) as an independent consistency check to validate the derived parameters. The detailed SED fitting process and the setup will be shown in Section 4.3.

Figure 3 presents the results of our multiband photometric decomposition using `GalfitS`. Crucially, the decomposition yields a clear and robust detection of the host galaxy, particularly in the F356W, F444W, F1000W, and F1280W filters where the stellar continuum is prominent. While the host is detected across the full instrument suite (with the exception of the F090W and F115W bands), these rest-frame optical-to-IR bands provide good constraints on the host galaxy emission, allowing the estimation of the host galaxy properties.

Interestingly, the decomposition resolves two components in the rest-frame UV bands: a central component colocated with the quasar, and an off-center component situated approximately 2 kpc away from the mass center determined from the long-wavelength filter. These clumps are similar to features seen in high-$z$ galaxies (e.g., K. Tadaki et al. 2018; S. Gillman et al. 2024), suggesting they may represent the star-forming regions in the early Universe. We also obtain a marginal detection in the F2100W filter (SNR $\approx 2$). At this rest-frame wavelength ($\sim$2.5 $\mu$m), the emission is dominated by the hot dust from the AGN, consistent with the diminishing contribution from the stellar population.

### 3.3. MIRI LRS and MRS

The MIRI LRS 1D spectrum was modeled using a methodology consistent with our analysis of the NIRSpec G395M data, employing a model comprised of a continuum and Gaussian emission lines. A diverse suite of emission features was identified, including He I, O I, and the Paschen series. To isolate the continuum, we performed a preliminary fit using a single power law after masking these emission regions. As the stellar and dust torus components are not negligible in the observed wavelength regime (see Section 4.3), we model the underlying continuum using a dual power-law formulation. In this framework, the first component characterizes the primary emission from the central engine, while the second accounts for the combined contributions from the host galaxy's stellar population and the thermal emission from the dust torus.

Subsequently, we model the identified emission features using the continuum-subtracted spectrum. Due to the limited spectral resolution of the MIRI LRS instrument (S. Kendrew et al. 2015), a detailed decomposition into narrow and broad components is generally omitted in favor of single Gaussian profiles to characterize line morphologies. An exception was made for the H$\alpha$ complex, which is modeled with a double-Gaussian profile utilizing empirical constraints derived from our NIRSpec observations. Parameter optimization was conducted via the `lmfit` Python package (M. Newville et al. 2014). To maintain maximal flexibility amidst the instrument's resolution limits, we allow the centroid, width, and amplitude of each line to vary independently rather than imposing tied kinematic constraints. This multistage approach culminated in a global fit of the MIRI LRS spectrum, employing a composite model of a continuum and Gaussian emission lines whose parameters are initialized from the results of the isolated fits. The final spectral decomposition is

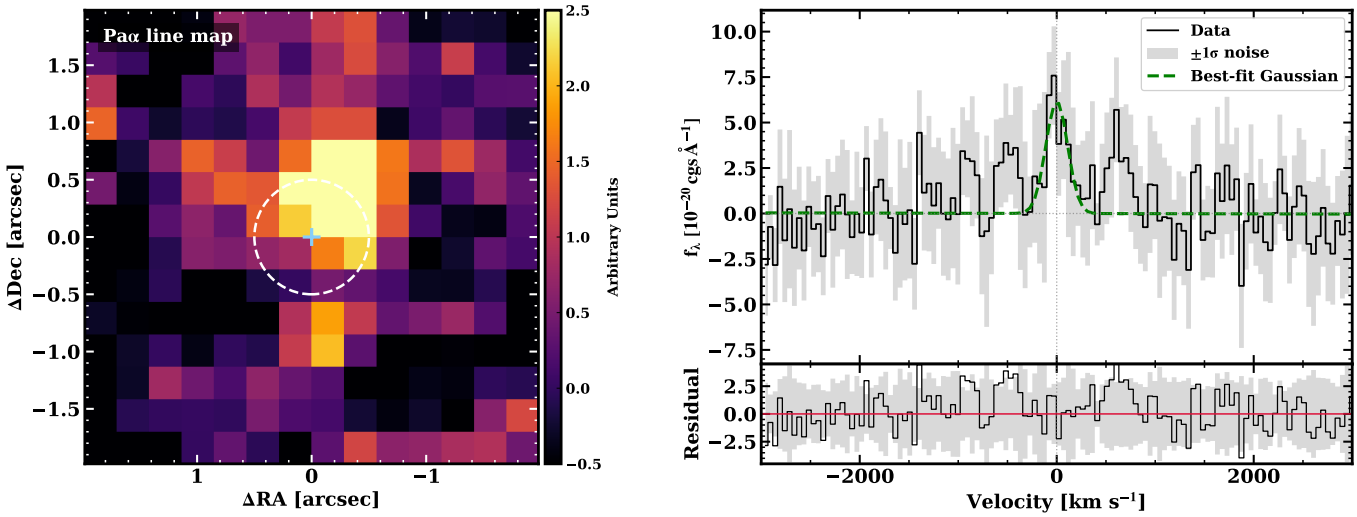



**Figure 4.** Left: the line intensity map generated from the MIRI MRS data around the Pa$\alpha$ emission, with a bandwidth of 1000 km s$^{-1}$. The light blue cross in the panel presents the locus of the quasar, and the dashed circle represents an aperture with a radius of 0.″5. Right: spectrum extracted from the central 0.″5 aperture of the MIRI observation. The upper panel shows the continuum-subtracted flux (solid black line) and associated error (gray-shaded region). The green dashed line shows the best-fit model. The bottom panel shows the residuals derived from subtracting the model from the observed data.

illustrated in Figure B1, with the derived physical parameters shown in Table 2.

Our spectral decomposition reveals that emission features at shorter rest-frame wavelengths, specifically He I $\lambda$7281, He I $\lambda$7816, and O I $\lambda$8446, exhibit marginally broader profiles relative to the Paschen series. However, we cannot definitively exclude the influence of instrumental broadening on these observed widths. The MIRI LRS resolving power is lower at the blue end of the spectrum ($R \sim 40$ at 5 $\mu$m) compared to the red end ($R \sim 160$ at 10 $\mu$m). Consequently, the current spectral resolution precludes a detailed kinematic analysis of these rest-frame near-infrared (NIR) line profiles.

For the MIRI MRS data, we perform a one-component Gaussian function to characterize the Pa$\alpha$ emission-line profiles, with a linear function to fit the background (see Figure 4). The final uncertainties in the fit parameters, such as FWHM, flux, and redshift, were obtained as the standard deviation of all the individual measurements of 1000 bootstrapped spectra after adding a random Gaussian noise equal to the rms to the original spectrum. The integrated Pa$\alpha$ flux is $(8.8 \pm 2.2) \times 10^{-18}$ erg s$^{-1}$ cm$^{-2}$ with an intrinsic FWHM of $230 \pm 100$ km s$^{-1}$. The redshift of the Pa$\alpha$ line is $7.1881 \pm 0.0008$, compatible with the one obtained from NIRSpec spectroscopy (see Table 2)

### 3.4. Dust Extinction

S. Fujimoto et al. (2022) characterized GNz7q as a high-redshift red quasar hosted by a dusty starburst, indicating that the observed emission from both the nuclear and stellar components is strongly suppressed by dust. With the new NIRSpec observations, we therefore quantify the dust attenuation ($A_V$). This derived extinction is subsequently applied to infer the intrinsic BH mass and the bolometric luminosity.

In the same manner as other high-$z$ AGNs studies (e.g., Y. Harikane et al. 2023), we estimate the dust attenuation for the quasar component via the Balmer decrement of the narrow emission lines (including the core component and the outflowing component; Table 1). Adopting a typical dust extinction law and an intrinsic, dust-free narrow-line ratio of $f_{\mathrm{H}\alpha}/f_{\mathrm{H}\beta} = 2.86$ (D. E. Osterbrock 1989; D. Calzetti et al. 2000), the observed ratio of $3.03^{+0.08}_{-0.07}$ yields an extinction of $A_V = 0.21^{+0.09}_{-0.08}$ mag, following the method proposed in A. Domínguez et al. (2013) and I. G. Momcheva et al. (2013).

To validate our extinction estimate, we performed an independent estimation based on continuum fitting. We modeled the observed rest-frame UV-to-optical SED using a composite quasar template (J. Selsing et al. 2016) reddened by a standard dust extinction law (D. Calzetti et al. 2000), treating the $A_V$ as a free parameter. The resulting $A_V$ is consistent with the value derived from the Balmer decrement of the narrow emission line, while it is different from that obtained from the Balmer decrement derived from the broad emission line ($A_V = 1.9$, assuming an intrinsic ratio of 3.06, which is a common value for local AGN; X. Dong et al. 2008). However, caution is warranted as the high gas densities characteristic of the BLR deviate from standard Case B recombination assumptions. Consequently, the elevated $A_V$ derived from broad lines is likely caused by collisional excitation rather than dust attenuation (S. Son et al. 2025; Z. Yan et al. 2026).

While Paschen-to-Balmer line ratios can offer an independent estimation for dust attenuation (N. A. Reddy et al. 2023), the application in this analysis is severely limited by the spectral resolution. Specifically, the low spectral resolution of MIRI LRS precludes the decomposition of Pa$\beta$ and Pa$\gamma$ into distinct broad (AGN) and narrow (host) kinematic components, a challenge further compounded by the blending of Pa$\gamma$ with He I $\lambda$10830. In contrast, the MIRI MRS data recover only the narrow Pa$\alpha$ component attributed to the host galaxy. Consequently, deriving a robust $A_V$ from these inconsistent spectral components is nontrivial. Although the observed Pa$\alpha$/Pa$\beta$ flux ratio is consistent with measurements of the BLR in high-$z$ quasars (S. E. I. Bosman et al. 2024; S. E. I. Bosman et al. 2025), we caution that this agreement may be fortuitous given the mixing of physical origins. Definitive constraints on the extinction will require deeper, high-resolution spectroscopy capable of resolving the underlying kinematic substructure.

**Table 1**
Properties of GNz7q

| Properties | Value | Unit |
|---|---|---|
| R.A. | 12:36:17.0 | |
| Decl. | +62:12:32.27 | |
| $z$ | 7.1899 | |
| | Spectral Fitting | |
| $\log L_{5100\,\text{Å}}$ | $45.02 \pm 0.01$ | erg s$^{-1}$ |
| $\alpha_1$ | $2.12 \pm 0.01$ | ⋯ |
| $\alpha_2$ | $1.83 \pm 0.01$ | ⋯ |
| $\text{FWHM}_{\text{Fe}}$ | $1039 \pm 14$ | km s$^{-1}$ |
| $f_{\text{Fe,4434-4684 Å}}$ | $1968 \pm 34$ | $10^{-20}$ erg s$^{-1}$ cm$^{-2}$ |
| $\text{FWHM}_{\text{H}\beta,\text{BLR}}$ | $2221 \pm 20$ | km s$^{-1}$ |
| $\text{FWHM}_{\text{H}\beta,\text{rBLR}}$ | $11184 \pm 30$ | km s$^{-1}$ |
| $f_{\text{H}\beta,\text{BLR}}$ | $932 \pm 30$ | $10^{-20}$ erg s$^{-1}$ cm$^{-2}$ |
| $f_{\text{H}\beta,\text{rBLR}}$ | $1381 \pm 100$ | $10^{-20}$ erg s$^{-1}$ cm$^{-2}$ |
| $f_{\text{H}\alpha,\text{BLR}}$ | $2080 \pm 87$ | $10^{-20}$ erg s$^{-1}$ cm$^{-2}$ |
| $f_{\text{H}\alpha,\text{rBLR}}$ | $10843 \pm 172$ | $10^{-20}$ erg s$^{-1}$ cm$^{-2}$ |
| $f_{\text{H}\gamma,\text{BLR}}$ | $366 \pm 21$ | $10^{-20}$ erg s$^{-1}$ cm$^{-2}$ |
| $f_{\text{H}\gamma,\text{rBLR}}$ | $838 \pm 47$ | $10^{-20}$ erg s$^{-1}$ cm$^{-2}$ |
| $\text{FWHM}_{[\text{OIII}]}$ | $193 \pm 8$ | km s$^{-1}$ |
| $f_{[\text{OIII}]}$ | $138 \pm 9$ | $10^{-20}$ erg s$^{-1}$ cm$^{-2}$ |
| $f_{[\text{OIII}],\text{of}}$ | $94 \pm 8$ | $10^{-20}$ erg s$^{-1}$ cm$^{-2}$ |
| $f_{\text{H}\alpha,\text{NLR}}$ | $461 \pm 26$ | $10^{-20}$ erg s$^{-1}$ cm$^{-2}$ |
| $f_{\text{H}\alpha,\text{of}}$ | $311 \pm 25$ | $10^{-20}$ erg s$^{-1}$ cm$^{-2}$ |
| $f_{\text{H}\beta,\text{NLR}}$ | $157 \pm 12$ | $10^{-20}$ erg s$^{-1}$ cm$^{-2}$ |
| $f_{\text{H}\beta,\text{of}}$ | $106 \pm 11$ | $10^{-20}$ erg s$^{-1}$ cm$^{-2}$ |
| $f_{\text{H}\gamma,\text{NLR}}$ | $44 \pm 9$ | $10^{-20}$ erg s$^{-1}$ cm$^{-2}$ |
| $f_{\text{H}\gamma,\text{of}}$ | $30 \pm 8$ | $10^{-20}$ erg s$^{-1}$ cm$^{-2}$ |
| | AGN Properties | |
| $\log M_{\text{BH}}$ | $7.55 \pm 0.34$ | $M_\odot$ |
| $\lambda_{\text{Edd}}$ | $2.7 \pm 0.4$ | ⋯ |
| $\log L_{\text{bol}}$ | $46.2 \pm 0.1$ | erg s$^{-1}$ |
| $A_V$ | $0.21^{+0.09}_{-0.08}$ | mag |
| | Host Galaxy Properties | |
| $\log M_*$ | $10.5 \pm 0.4$ | $M_\odot$ |
| $\log L_{\text{FIR}}$ | $12.3 \pm 0.3$ | $L_\odot$ |
| $\text{SFR}_{\text{Pa}\alpha}$ | $250 \pm 88$ | $M_\odot$ yr$^{-1}$ |
| $\text{SFR}_{\text{FIR}}$ | $330 \pm 97$ | $M_\odot$ yr$^{-1}$ |
| $\log L_{[\text{CII}]}$[a] | $(1.1 \pm 0.3) \times 10^9$ | $L_\odot$ |
| $\text{FWHM}_{[\text{CII}]}$[a] | $280 \pm 40$ | km s$^{-1}$ |

**Notes.** Properties of this source, including the spectra and SED fitting results.
[a] Values are adopted from S. Fujimoto et al. (2022).

The $A_V$ of the AGN can also be constrained by photometrically comparing the rest-frame UV–optical SED shape of GNz7q with standard quasar templates (J. Selsing et al. 2016; N. Kato et al. 2020; J. Yang et al. 2021). We also employed this approach to estimate the intrinsic dust reddening. We note that, while the shape of the rest-frame optical continuum of GNz7q is similar to that of typical high-$z$ quasars, the rest-frame UV continuum exhibits a divergent slope distinct from the standard population. This spectral discrepancy suggests a nonstandard extinction curve for the central AGN, which cannot be well modeled with a typical extinction curve (e.g., D. Calzetti et al. 2000; D. Calzetti 2001; K. D. Gordon et al. 2003). Such properties have been observed in other high-$z$ systems (S. Gallerani et al. 2010; R. L. Sanders et al. 2025), which may be attributable to specific dust formation mechanisms in quasars (R. Maiolino et al. 2004; F. Di Mascia et al. 2021). A comprehensive analysis of this anomalous extinction curve is beyond the scope of the current work and will be presented in a separate paper (Q. Fei et al. 2026, in preparation). Consequently, we adopt the value derived from the narrow emission lines, $A_V = 0.21^{+0.09}_{-0.08}$, as the fiducial extinction parameter for the subsequent analyses. This is the most conservative value in terms of the bolometric luminosity and BH mass estimate.

## 4. Results and Discussion

### 4.1. BH Properties

We then estimate the BH properties using the parameters derived from the best-fit model for the spectrum. In particular, the $M_{\text{BH}}$ of an AGN is calculated using the virial estimator

$$M_{\text{BH}} = f_{\text{BLR}} \frac{R_{\text{BLR}} \Delta V^2}{G}, \quad (1)$$

where $G$ is the gravitational constant, $R_{\text{BLR}}$ is the radius of the BLR, and $f_{\text{BLR}}$ is the virial factor, a dimensionless coefficient that accounts for the unknown geometry, kinematics, and inclination angle of the BLR. The velocity, $\Delta V$, is estimated using the width of the broad emission line (e.g., $\sigma_{\text{BLR}}$ or $\text{FWHM}_{\text{BLR}}$). The measurement of $R_{\text{BLR}}$ is commonly conducted by reverberation mapping (RM), which measures the time lag between variations in the continuum flux and the subsequent response of the broad emission lines (e.g., P. Du et al. 2016). We adopt a virial factor of $f_{\text{BLR}} = 4.16$ to match the use of $\sigma_{\text{BLR}}$ in our paper, based on the RM of SDSS quasars (Y. Shen et al. 2024), assuming that the BLR geometry of GNz7q is consistent with that of local AGNs. These RM studies have demonstrated a robust correlation between the BLR size ($R_{\text{BLR}}$) and the AGN's luminosity. The luminosity is typically quantified by either the 5100 Å monochromatic luminosity ($L_{5100}$) or the broad-line luminosity ($L_{\text{BLR}}$). This established radius–luminosity relationship allows for the calibration of single-epoch virial mass estimators. These empirical formulae, which are benchmarked using AGNs in the local Universe (e.g., J. E. Greene & L. C. Ho 2005; M. Vestergaard & B. M. Peterson 2006; A. E. Reines & M. Volonteri 2015), enable the estimation of $M_{\text{BH}}$ using the line widths and luminosities measured from a single spectrum even for high-$z$ AGNs.

Initially identified as a Compton-thick, super-Eddington candidate exhibiting significant X-ray faintness (S. Fujimoto et al. 2022), this source suggests that BH mass estimators derived from local, lower-accretion AGNs may require modification. The RM analyses have revealed that the canonical luminosity–size relation, which is calibrated on local AGNs with moderate accretion rates, is not universally applicable (P. Du et al. 2015, 2016, 2018) and is regulated by the accretion rate. This is caused by the theoretical prediction that the canonical BLR framework from the photoionizing model, $R_{\text{BLR}} \propto L_{\text{ion}}^{1/2}$, where $R_{\text{BLR}}$ is the size of the BLR and $L_{\text{ion}}$ is the luminosity of the ionizing source, requires a specific structure of the BLR, which may be modified when the accretion rate exceeds the Eddington ratio (J.-M. Wang et al. 2014; B. Czerny et al. 2019). Studies targeting massive BHs with higher accretion rates in the local Universe have found that these objects exhibit H$\beta$ time lags that are systematically shorter by factors of ∼2–8 than predicted by the canonical

relation for given luminosities (P. Du et al. 2015, 2016, 2018). The statistical analysis of these local AGNs confirmed that the magnitude of this lag shortening strongly correlates with the accretion rate (P. Du et al. 2016, 2018). A physical explanation for this discrepancy is the self-shadowing effect of a slim accretion disk, which is expected to form in super-Eddington regimes (e.g., J.-M. Wang et al. 2014). In this model, the inner part of the disk becomes geometrically thick due to intense radiation pressure. This inflated disk then anisotropically shields the BLR from ionizing photons, causing the H$\beta$ ionization front to shrink. Given this established dependency, applying the canonical $R_{\rm BLR}$–$L_{5100}$ relation to a high accretion rate object would result in an erroneous $R_{\rm BLR}$, and consequently, a BH mass that needs modification (R. Abuter et al. 2024).

To estimate the BH mass, we first determine the BLR size using Equation (6) of P. Du et al. (2015) with the H$\beta$-based empirical relationship, which explicitly accounts for the Eddington ratio. This relation takes the form

$$\log\left(\frac{R_{\rm BLR,H\beta}}{\text{lt-day}}\right) = \alpha + \beta \log\left(\frac{L_{\rm H\beta}}{10^{42}\ \text{erg s}^{-1}}\right), \quad (2)$$

where the coefficients, $\alpha = 1.21 \pm 0.06$ and $\beta = 0.53 \pm 0.06$ are taken from P. Du et al. (2015), by assuming the super-Eddington accretion rate from S. Fujimoto et al. (2022). We then calculate the BH mass using this BLR size, a typical virial parameter, and an assumed high accretion rate of $\dot{\mathcal{M}} \geqslant 3$ (S. Fujimoto et al. 2022). This procedure, incorporating the dust extinction correction of $A_V = 0.21$, yields a mass for GNz7q of $\log(M_{\rm BH}/M_\odot) = 7.55 \pm 0.34$. The uncertainty is mainly contributed by the systematic uncertainty embedded within the calibrator, which is 0.31 dex (Y. Shen et al. 2024). This value is approximately two orders of magnitude lower than typical quasars at $z \gtrsim 6$ (X. Fan et al. 2023) and is consistent with the high-mass end of the BH mass function for the faint JWST-detected AGN population (J. Matthee et al. 2024; A. J. Taylor et al. 2025a).

To validate our results, we cross-check the BH mass using two independent empirical relations. First, applying the continuum-based estimator of P. Du et al. (2018),

$$\log\left(\frac{R_{\rm BLR,H\beta}}{\text{lt-day}}\right) = \alpha + \beta \log\left(\frac{L_{5100}}{10^{44}\ \text{erg s}^{-1}}\right), \quad (3)$$

with coefficients $\alpha = 1.32 \pm 0.06$ and $\beta = 0.53 \pm 0.06$ from P. Du et al. (2018), yields $\log(M_{\rm BH}/M_\odot) = 7.60 \pm 0.40$. Second, using the Fe II-based size–luminosity relation (e.g., P. Du & J.-M. Wang 2019; J. Maithil et al. 2022; Z. Pan et al. 2025) results in $\log(M_{\rm BH}/M_\odot) = 7.55 \pm 0.40$. Both values are in agreement with our primary Eddington ratio corrected H$\beta$ estimate. This consistency indicates that the scaling between the BLR and continuum luminosities follows the empirical relationships established for the local Universe (J. E. Greene & L. C. Ho 2005), suggesting that GNz7q possesses a BLR structure comparable to typical low-redshift AGNs (S. E. I. Bosman et al. 2024; S. E. I. Bosman et al. 2025). We further assess the measurement of our fiducial mass by comparing it with single-epoch virial BH mass estimates (J. E. Greene & L. C. Ho 2005; A. E. Reines & M. Volonteri 2015). Applying Equation (10) of J. E. Greene & L. C. Ho (2005) yields a comparable value of $\log(M_{\rm BH}/M_\odot) \simeq 7.5$, while Equation (1) of A. E. Reines & M. Volonteri (2015) returns a marginally larger value of $\log(M_{\rm BH}/M_\odot) \simeq 7.8$. Both estimates agree with the P. Du et al. (2016) estimation within the ∼0.3 dex systematic uncertainty (Y. Shen et al. 2024). Given that the ionizing accretion disk is spatially compact relative to the BLR radius, we adopt the Eddington ratio-corrected, H$\beta$-based determination as our fiducial mass.

**Table 2**
GNz7q Properties and Results from MIRI Data

| Properties | Value | Unit |
|---|---|---|
| $f_{\rm HeI\lambda7281}$ | $1683 \pm 271$ | $10^{-20}$ erg s$^{-1}$ cm$^{-2}$ |
| $f_{\rm HeI\lambda7816}$ | $2068 \pm 370$ | $10^{-20}$ erg s$^{-1}$ cm$^{-2}$ |
| $f_{\rm HeI\lambda10031}$ | $<280$ | $10^{-20}$ erg s$^{-1}$ cm$^{-2}$ |
| $f_{\rm HeI\lambda10830}$ | $508 \pm 208$ | $10^{-20}$ erg s$^{-1}$ cm$^{-2}$ |
| $f_{\rm OI\lambda8446}$ | $2179 \pm 303$ | $10^{-20}$ erg s$^{-1}$ cm$^{-2}$ |
| $f_{\rm Pa\gamma}$ | $427 \pm 212$ | $10^{-20}$ erg s$^{-1}$ cm$^{-2}$ |
| $f_{\rm Pa\beta}$ | $631 \pm 269$ | $10^{-20}$ erg s$^{-1}$ cm$^{-2}$ |
| $f_{\rm Pa\alpha}$ | $880 \pm 220$ | $10^{-20}$ erg s$^{-1}$ cm$^{-2}$ |

**Note.** Derived physical properties of rest-frame NIR emission lines from the MIRI spectra. Due to the instrumental broadening and limited spectral resolution, intrinsic line widths are omitted. All nondetections are reported as $2\sigma$ upper limits. Given the poor spectral resolution of the MIRI LRS, no FWHM of those emission lines is shown.

The abovementioned BH mass estimate already considers the effect of the dust extinction. Given the relatively low $A_V$ in the rest-frame optical ($A_V = 0.21^{+0.09}_{-0.08}$), the corrected broad H$\beta$ flux of $f_{\rm H\beta,BLR} = 1039 \pm 30 \times 10^{-20}$ erg s$^{-1}$ cm$^{-2}$. Due to the shallow dependence of the virial mass on luminosity ($M_{\rm BH} \propto L^{0.5}$), this correction corresponds to a marginal increase in the BH mass of approximately 5% (∼0.02 dex), which falls well within the systematic uncertainties.

We derive a bolometric luminosity of $L_{\rm bol} = (1.50 \pm 0.20) \times 10^{46}$ erg s$^{-1}$ from the best-fit SED. Taking uncertainties into account, this is in good agreement with the value of $(1.0 \pm 0.3) \times 10^{46}$ erg s$^{-1}$ inferred from the 5100 Å monochromatic luminosity using the bolometric correction of S. Kaspi et al. (2000). The Eddington ratio ($\lambda_{\rm Edd}$) was then calculated as (B. Trakhtenbrot et al. 2011)

$$\lambda_{\rm Edd} = \frac{L_{\rm bol}/\text{erg s}^{-1}}{1.5 \times 10^{38} M_{\rm BH}/M_\odot}, \quad (4)$$

where $1.5 \times 10^{38} M_{\rm BH}/M_\odot$ is the Eddington luminosity of the BH. Based on the derived luminosity and the fiducial BH mass, the source is characterized by a highly super-Eddington ratio of $\lambda_{\rm Edd} = 2.7 \pm 0.4$.

Evidence for super-Eddington accretion is further strengthened by the identification of the O I$\lambda$8446 emission (Figure B1; Table 2). As detailed by K. Inayoshi et al. (2022), this low-ionization feature primarily originates from a dense gaseous disk ($0.1 \lesssim r \lesssim 1$pc) close to the central massive BH. Such broad [O I] lines powered by AGNs were also discovered in recent faint AGNs (little red dots (LRDs)) discovered by JWST (V. Kokorev et al. 2026; R. Tripodi et al. 2025; W. Q. Sun et al. 2026)

In Figure 5, we show the BH mass and bolometric luminosity relation of GNz7q by plotting its location on the $L_{\rm bol}$–$M_{\rm BH}$ plane alongside other AGNs in the early Universe ($z > 4$). For

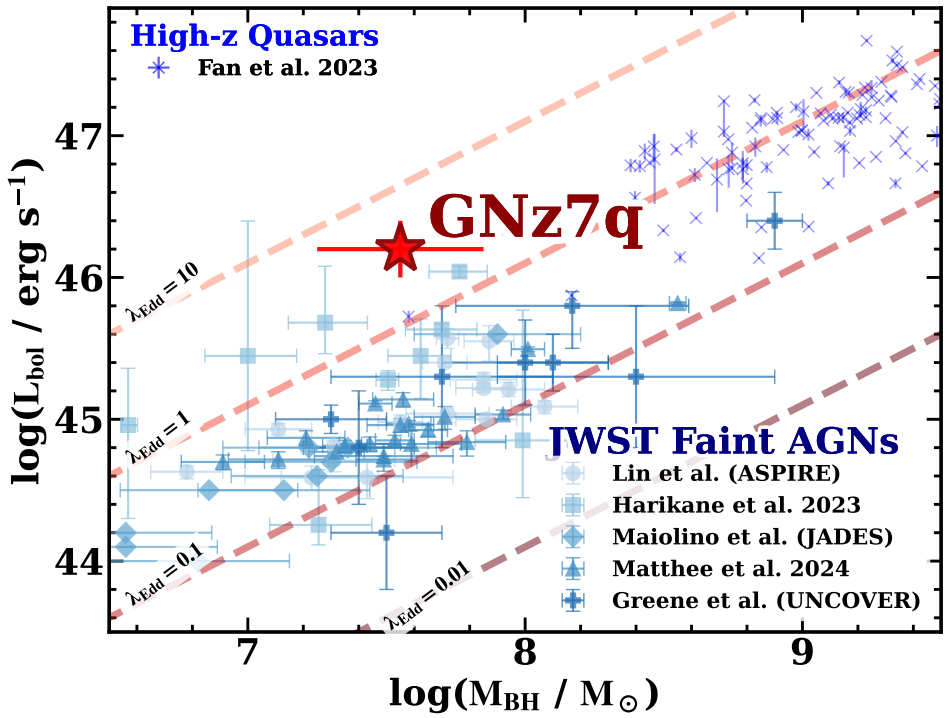



**Figure 5.** BH mass vs. bolometric luminosity of GNz7q and other AGNs at $z > 4$, including the quasars discovered by ground-based facilities (Y. Shen et al. 2019; S. L. Reed et al. 2019; J. Yang et al. 2021; E. P. Farina et al. 2022) and the JWST-discovered faint AGNs (J. E. Greene et al. 2024; Y. Harikane et al. 2023; R. Maiolino et al. 2024b; J. Matthee et al. 2024; X. Lin et al. 2024).

comparison, we also show highly luminous quasars so far discovered with ground-based facilities and the emerging population of faint AGNs recently identified with JWST, at similar redshifts with GNz7q ($z > 4$) compiled from the literature (Y. Shen et al. 2019; J. Yang et al. 2021; E. P. Farina et al. 2022; J. Matthee et al. 2024; Y. Harikane et al. 2023; J. E. Greene et al. 2024; X. Lin et al. 2024; R. Maiolino et al. 2024b). Our analysis demonstrates that GNz7q is placed in the highest $\lambda_{\rm Edd}$ regime among the quasar/AGN populations so far identified at $z > 4$. This significantly elevated accretion rate implies that the source is undergoing a phase of rapid mass assembly, consistent with the evolutionary pathway required to form the most massive SMBHs observed at $z \sim 6$.

### 4.2. X-Ray Faintness

The nature of GNz7q as a candidate for a Compton-thick quasar at $z > 7$ was initially suggested by its nondetection in one of the deepest Chandra X-ray surveys, despite its high luminosity in the infrared (S. Fujimoto et al. 2022). This phenomenon of X-ray faintness has recently become a recurring theme in JWST observations, particularly among the emerging population of LRDs and faint broad-line AGNs (e.g., R. Maiolino et al. 2025). Motivated by this context, we revisit the X-ray properties of GNz7q utilizing our updated bolometric luminosity ($L_{\rm bol}$) estimate. Adopting an intrinsic X-ray photon index of $\Gamma = 2.0$ that follows the relation $N(E) \propto E^{-\Gamma}$, where $E$ is the energy of photons and $N(E)$ represents the X-ray spectrum, we derive an upper limit of $L_{2-10\ \rm keV} < 2.9 \times 10^{42}$ erg s$^{-1}$. Figure 6 compares GNz7q against the empirical relation between the bolometric-to-X-ray luminosity ratio ($k_{\rm bol} \equiv L_{\rm bol}/L_{2-10\ \rm keV}$) and bolometric luminosities (F. Duras et al. 2020). We also present other high-$z$ AGNs as the comparison sample (e.g., F. Wang et al. 2021b; R. Maiolino et al. 2025). We find that GNz7q

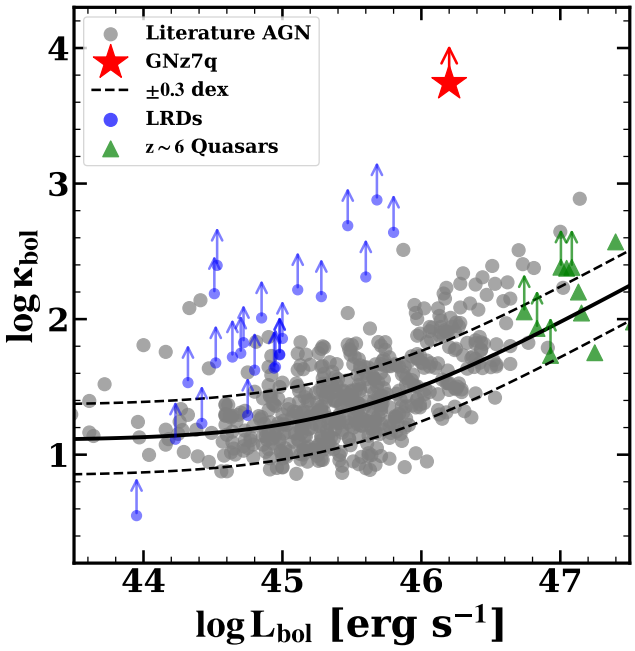



**Figure 6.** Unique X-ray faintness of GNz7q, compared to other AGNs in the literature. GNz7q is shown as a red star. Comparison samples include $z \sim 2$ quasars (gray points; E. Lusso et al. 2010), high-$z$ Type 1 faint AGNs, mainly little red dots (blue circles; R. Maiolino et al. 2025), and luminous quasars at $z \gtrsim 6$ (green triangles; F. Wang et al. 2021b). The black solid line shows the empirical relationship between $k_{\rm bol}$ and $L_{\rm bol}$ from F. Duras et al. (2020).

deviates from standard quasar scaling relations at a confidence level of $>5\sigma$. While this suppression generally mirrors the X-ray faint AGN population identified by JWST, GNz7q is far more extreme, exhibiting a deviation $\sim$1 dex deeper than even this faint population. This profound faintness reinforces the link

between GNz7q and the most heavily obscured, rapidly growing BHs in the early Universe.

Two physical mechanisms may account for this observed X-ray weakness. First, intrinsic X-ray production may be suppressed by the super-Eddington accretion flow. In this regime, the inner accretion disk becomes geometrically thick ("slim disk"), which can anisotropically shield the X-ray corona or prevent the formation of a standard reprocessing region due to self-shadowing effects (P. Madau & F. Haardt 2024; K. Inayoshi et al. 2025). Alternatively, the suppression may be extrinsic, resulting from heavy obscuration by a Compton-thick column ($N_{\rm H} \approx 10^{24}\,{\rm cm}^{-2}$) that blocks line-of-sight X-rays (R. Maiolino et al. 2025). Given the source's high Eddington ratio and its location within a dusty starburst host, it is plausible that a combination of both intrinsic super-Eddington suppression and high column density obscuration contributes to the observed properties. Our finding is broadly consistent with the theoretical framework that interprets the systematic X-ray faintness of high-redshift AGNs as a natural signature of super-Eddington accretion (e.g., A. Trinca et al. 2026a). In this model, the geometrically thick slim disk configuration that operates at $\lambda_{\rm Edd} \gtrsim 1$ intrinsically suppresses the coronal X-ray output and shifts the predicted $k_{\rm bol}$–$L_{\rm bol}$ locus systematically upward for the most rapidly accreting objects. The extreme deviation we measure for GNz7q ($\lambda_{\rm Edd} = 2.7$, $k_{\rm bol}$ offset $\gtrsim 5\sigma$ above the F. Duras et al. 2020 relation) is quantitatively in line with this prediction, providing an alternative explanation to the observed X-ray weakness without invoking a purely Compton-thick geometry.

### 4.3. Host Galaxy Properties

To accommodate both AGN and host galaxy components in GNz7q, we also use the `cigale` code for our SED fitting (M. Boquien et al. 2019; G. Yang et al. 2022). In this analysis, we fix the redshift at $z = 7.1899$ and include all the FIR and mm photometry observed with Herschel, SCUBA-2, and NOEMA presented in S. Fujimoto et al. (2022). For the stellar component, we adopt the single stellar population models of G. Bruzual & S. Charlot (2003) (`bc03` module), assuming a G. Chabrier (2003) IMF. The SFH is modeled using a delayed-$\tau$ function. We also include a burst component in the model whose SFH can be modeled as an exponential profile. The mass fraction of the late starburst population is allowed to vary between 0 and 0.5 in steps of 0.1. Following the procedures of M.-Y. Zhuang & L. C. Ho (2023) and T. S. Tanaka et al. (2025), we set an upper limit on the age of the stellar population, requiring it to be less than 95% of the age of the universe at the galaxy's redshift ($t_{\rm age} \leqslant 0.95\,t_{\rm H}$). We include contributions from ionized gas using the `nebular` module. To account for the potentially extreme interstellar medium (ISM) conditions in high-redshift galaxies, we allow the ionization parameter ($\log U$) to vary between $-3$ and $-1$ and the gas-phase metallicity to range from 10% to 100% of the solar value. The dust attenuation is also included in the fitting, following a modified D. Calzetti et al. (2000) attenuation law (`dustatt_modified_starburst` module). Given the confirmed presence of broad lines in our source, we include an AGN component using the default `skirtor` module in `cigale` (M. Stalevski et al. 2016; M. Boquien et al. 2019). We fix the viewing angle to a face-on orientation ($i = 0°$) in the fitting and let AGN emission vary uniformly from 0.1 to 0.9 in the rest-frame UV-to-optical band (1000–10000 Å).

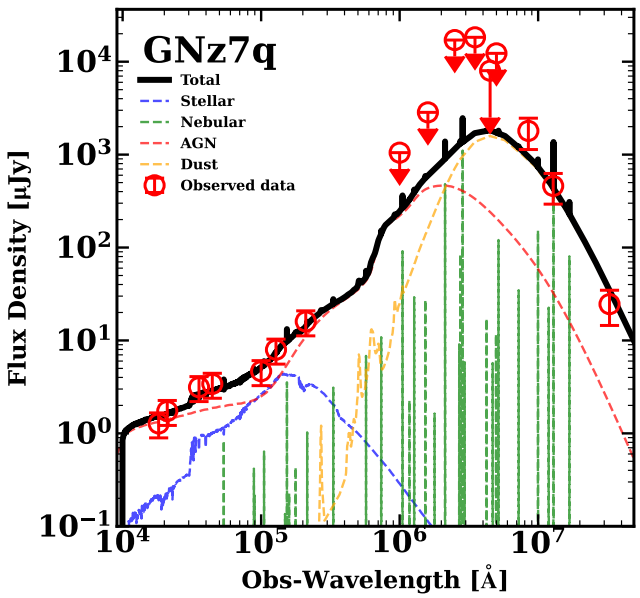



**Figure 7.** Best-fit multicomponent SED decomposition obtained using the `cigale` code. The observed photometry is shown as red points, comprising both the new JWST observations and archival data (S. Fujimoto et al. 2022). Dashed lines indicate the individual model components, including stellar population (blue), nebular emission (green), AGN (red), and cold dust (yellow). The solid black line represents the total integrated emission model.

In Figure 7, we present our best-fit SED with `cigale` (black), together with the individual components of stellar (blue), nebular (green), AGN (red), and thermal dust emission (yellow) from the stellar component. Our best-fit results suggest that the rest-frame UV-to-optical regime is dominated by the AGN continuum, which is consistent with the independent galaxy+AGN composite SED fitting presented in S. Fujimoto et al. (2022). In the rest-frame NIR bands, the stellar emission can be comparable to the AGN emission, which is consistent with our 2D decomposition results. In the rest-frame MIR regime, the emission is subsequently dominated by thermal emission from the hot dust torus, which is also consistent with the absence of the residual component in the F1800W map after subtracting the point-source component (Figure 3). At the longest wavelengths in the rest-frame FIR band, the SED is primarily shaped by the thermal emission originating from cold dust associated with the star-forming activity of the host galaxy. The SED fitting yields a host stellar mass of $\log(M_*/M_\odot) = 10.5 \pm 0.4$, and a star formation rate of ${\rm SFR} = 330 \pm 97\,M_\odot\,{\rm yr}^{-1}$.

We also estimated the SFR using the Pa$\alpha$ emission line with the MIRI spectrum. The spectrum was extracted from a circular aperture with a 0.″5 radius to capture the central emission region. We modeled the emission feature using a single Gaussian profile superimposed on a polynomial continuum (Figure 4). Notably, the intrinsic line width of the Pa$\alpha$ (FWHM $= 230 \pm 100\,{\rm km\,s}^{-1}$) is comparable to the [C II] emission line from the NOEMA observation (FWHM $= 280 \pm 40\,{\rm km\,s}^{-1}$, Table 1, S. Fujimoto et al. 2022), and indicates that a broad component is not required to describe the observed Pa$\alpha$ line profile, suggesting the emission is dominated by star formation. We measured an integrated Pa$\alpha$ flux of $88 \pm 22 \times 10^{-19}\,{\rm erg\,s}^{-1}\,{\rm cm}^{-2}$, which implies an SFR of $250 \pm 88\,M_\odot\,{\rm yr}^{-1}$. This spectroscopic estimate aligns with the

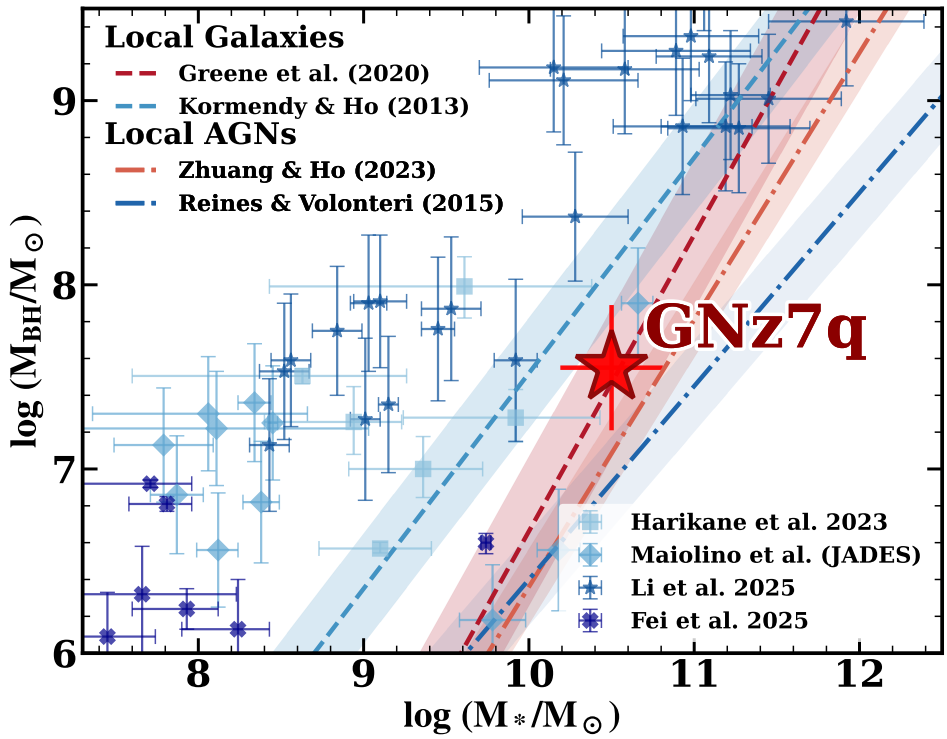



**Figure 8.** BH mass vs. stellar mass for GNz7q and other high-$z$ AGNs, including the JWST-discovered faint AGNs at $z \gtrsim 4$ (Y. Harikane et al. 2023; R. Maiolino et al. 2024b; Q. Fei et al. 2026) and luminous quasars at $z \sim 6$ (X. Fan et al. 2023; J. Yang et al. 2023; R. Li et al. 2026). The dashed and dotted lines represent the empirical relationships for the local galaxies (J. Kormendy & L. C. Ho 2013; J. E. Greene et al. 2020) and the local AGNs (A. E. Reines & M. Volonteri 2015; M.-Y. Zhuang & L. C. Ho 2023), respectively. GNz7q is shown as the red star.

SFR derived from our broadband SED fitting within the uncertainties, confirming that the host galaxy of GNz7q is undergoing vigorous star formation.

However, we note that the current SED fit yields a lower $L_{\rm IR}$ and $\rm SFR_{IR}$ compared to previous estimates ($L_{\rm IR} = (1.6 \pm 0.3) \times 10^{13} L_{\odot}$; S. Fujimoto et al. 2022), possibly due to an underprediction of the SCUBA 850 $\mu$m flux (Figure 7). Previous work derived the $\rm SFR_{IR}$ using a modified blackbody fit applied only to the FIR photometry, a method that bypasses the complexities of enforcing energy balance against a quasar-dominated UV/optical continuum. That approach successfully reproduced the 850 $\mu$m excess, resulting in a higher inferred $L_{\rm IR}$. It is worth noting that discrepancies where $\rm SFR_{IR} > SFR_{Pa\alpha}$ have been observed in high-$z$ dusty galaxies (J. Álvarez-Márquez et al. 2023; A. Bik et al. 2024). This excess suggests either that heavy obscuration is attenuating even the Paschen lines, or that we are witnessing a difference in star formation timescales, where Pa$\alpha$ traces instantaneous activity ($\sim$10 Myr) while the FIR emission integrates heating over a longer period ($\sim$100 Myr).

### 4.4. $\rm M_{BH}$–$\rm M_*$ Relation

The observed tight scaling relations between $M_{\rm BH}$ and host galaxy bulge properties, such as the $M_{\rm BH}$–$\sigma$ and $M_{\rm BH}$–$M_{\rm bulge}$ correlations (J. Magorrian et al. 1998; L. Ferrarese & D. Merritt 2000; K. Gebhardt et al. 2000; J. Kormendy & L. C. Ho 2013), indicate a fundamental coevolutionary pathway linking these components (P. Madau & M. Dickinson 2014). A similar, albeit more dispersed, correlation is also established between $M_{\rm BH}$ and the total stellar mass ($M_*$) (e.g., A. E. Reines & M. Volonteri 2015). This coupled growth is hypothesized to be particularly critical during the earlier phases of galaxy and BH formation. However, contrasting with these well-established local benchmarks, AGNs observed at high redshifts ($4.5 < z < 7$) present a significant deviation. These high-$z$ sources systematically populate the region above the extrapolated local $M_{\rm BH}$–$M_*$ relationship and are characterized by significant scatter (e.g., Y. Harikane et al. 2023; R. Maiolino et al. 2024b).

A prevailing explanation for this discrepancy has been observational selection bias, where flux-limited surveys are inherently biased toward detecting only the most luminous and massive BHs whose emission outshines that of their host galaxy (e.g., Y. Shen et al. 2015; J. Li et al. 2021, 2025; J. Silverman et al. 2025; T. S. Tanaka et al. 2025). However, recent deep JWST surveys focusing on low-luminosity AGNs at high redshift have argued that this selection effect is insufficient to fully account for the large observed offset, implying a genuine physical difference in the galaxy-BH connection at high redshift (e.g., F. Pacucci et al. 2023; R. Maiolino et al. 2024b; M. A. Stone et al. 2024).

Based on the derived $M_{\rm BH}$ and $M_*$, we calculate a mass ratio of $M_{\rm BH}/M_* = 0.1\%$, and the $M_{\rm BH}$–$M_*$ relation for GNz7q as well as other high-$z$ AGNs are shown in Figure 8. Our analysis demonstrates that the derived $M_{\rm BH}$ and $M_*$ values align with the established $M_{\rm BH}$–$M_*$ scaling relationship defined in the local Universe (e.g., J. Kormendy & L. C. Ho 2013; J. E. Greene et al. 2020). This consistency suggests that some AGN-galaxy systems can achieve a state of coevolutionary maturity as early as $z \sim 7$ (J. Li et al. 2025; M. Onoue et al. 2025; J. Silverman et al. 2025).

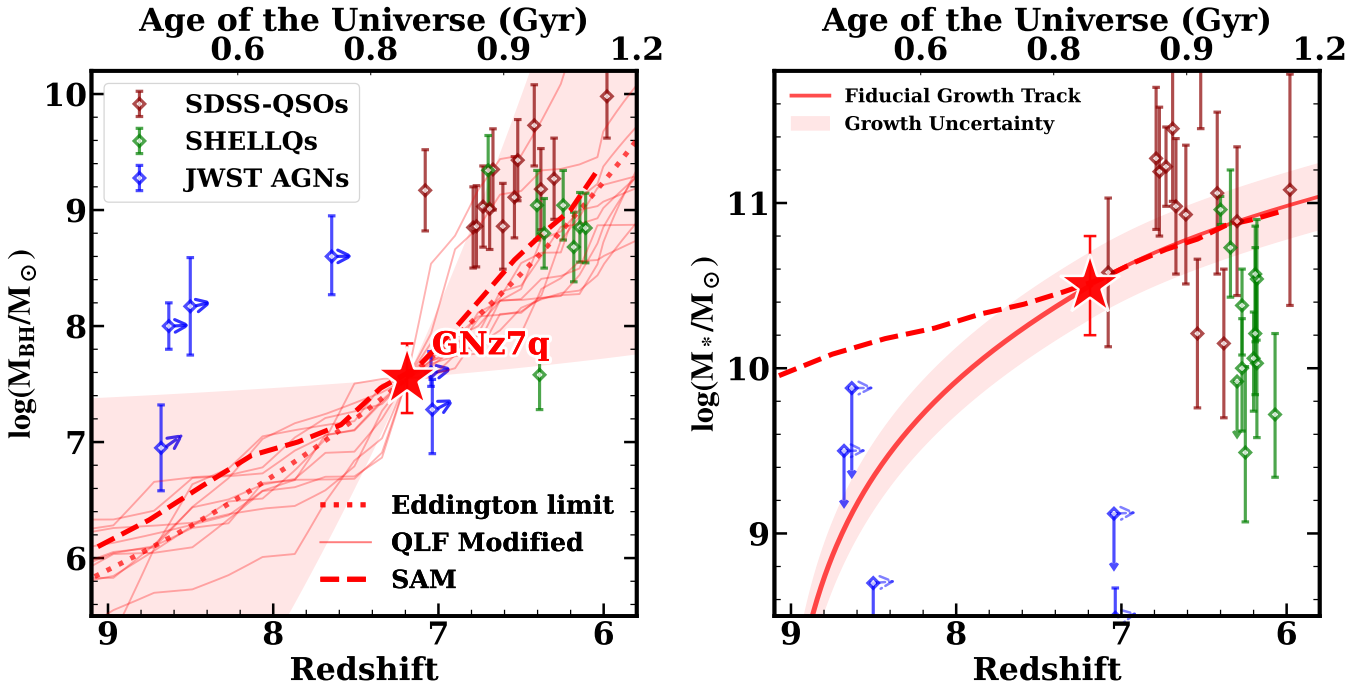



**Figure 9.** Evolutionary pathways of GNz7q and comparative high-$z$ samples. Left: $M_{\rm BH}$ vs. redshift. The dark-red, green, and blue diamonds denote luminous quasars (X. Fan et al. 2023), low-luminosity quasars selected from Subaru HSC (e.g., Y. Matsuoka et al. 2018; M. Onoue et al. 2025) and JWST faint AGNs (e.g., V. Kokorev et al. 2023; H. B. Akins et al. 2025; L. J. Furtak et al. 2024; R. L. Larson et al. 2023; A. J. Taylor et al. 2025b), respectively. Theoretical evolutionary tracks are adopted from W. Li et al. (2024) (light-red solid line) and the DELPHI semi-analytic model (red dashed line; P. Dayal et al. 2019). The red dotted line indicates a baseline assuming continuous Eddington-limited accretion ($\lambda_{\rm Edd} = 1$), with the red-shaded region denoting the possible region with $0.1 < \lambda_{\rm Edd} < 2.7$. Right: $M_*$ vs. redshift for our targets and comparison sample. The red-shaded region shows the mass growth for GNz7q host galaxy based on the SFH derived from the SED fitting (Table 1), and the red-shaded line represents the growth track of $M_*$ from DELPHI semi-analytic model.

### 4.5. Potential Evolutionary Pathway

The suite of derived physical parameters, including $M_{\rm BH}$ and $\lambda_{\rm Edd}$, alongside the $M_*$ and SFR, affords crucial constraints on the system's evolutionary trajectory. When compared with other high-$z$ AGNs, specifically the luminous ground-based quasars and the faint AGNs detected by JWST, this source occupies an intermediate locus in the census of $M_{\rm BH}$ and $M_*$, i.e., $M_{\rm BH}$ and $M_*$ of GNz7q are greater than those of faint AGNs while smaller than luminous quasars. More importantly, GNz7q is characterized by rapid dual growth in the manner of both BH and host galaxy, driven by high Eddington ratios and substantial star formation activity. This unique feature suggests that GNz7q represents a distinct phase on the BH–galaxy coevolutionary track.

To investigate the potential evolutionary trajectory of GNz7q, we model the evolution of its $M_{\rm BH}$ and $M_*$ as a function of cosmic time. We investigate the evolutionary tracks of BH mass using two physically motivated theoretical frameworks and one simplified baseline. First, we employ the quasar luminosity function (QLF)-regulated growth model presented in W. Li et al. (2024), which reconstructs BH growth via episodic accretion calibrated against the observed luminosity functions at high redshift. Second, we utilize the semi-analytic DELPHI framework (P. Dayal et al. 2019). We contrast these realistic scenarios with a simple model assuming continuous accretion at a constant Eddington ratio of unity ($\lambda_{\rm Edd} = 1$). Regarding the host galaxy assembly, we adopt a simplified assumption of growth via a continuous, constant SFR. While we recognize that reconstructing the full SFH offers a more realistic perspective (e.g., M. Onoue et al. 2025), we opt for the constant SFR approximation to mitigate the substantial uncertainties currently inherent in constraining detailed SFHs at these redshifts. For comparison, we also calculate the corresponding evolutionary paths for other AGN populations, including highly luminous ground-based quasars and faint AGNs, following the methodology detailed in R. Li et al. (2026). The $M_{\rm BH}$ and accretion rates are adopted from previous studies (e.g., R. L. Larson et al. 2023; V. Kokorev et al. 2023; L. J. Furtak et al. 2024; R. Tripodi et al. 2025). The SFRs for these high-$z$ AGN host galaxies are determined by combining literature values derived from the rest-UV luminosities with recent average constraints obtained from Atacama Large Millimeter/submillimeter Array observations (e.g., C. M. Casey et al. 2025).

Figure 9 presents the modeled evolutionary tracks for GNz7q and the faint AGN comparison sample at $z > 7$. Assuming a realistic SFR and the $\dot{M}_{\rm BH}$, the modeled evolution for GNz7q demonstrates a potential increase in $M_{\rm BH}$ by approximately 1 dex (with a maximum of $\sim$2 dex) and an increase in $M_*$ by $\sim$0.5 dex. This modeled growth path converges with the locus of luminous quasars observed in large surveys (e.g., SDSS, Subaru Hyper Suprime-Cam (HSC)) at $z \gtrsim 6$, suggesting that GNz7q is a likely progenitor for these massive systems.

In contrast, we find that the faint AGNs recently discovered by JWST at similar or higher redshifts are challenging to connect as being the direct progenitors of the SDSS-like quasars. For the BH mass, though their large masses make them possible for them to become SMBH at $z \sim 6$ (R. L. Larson et al. 2023; A. J. Taylor et al. 2025a), the BH mass measurements still have large uncertainties due to distinct models (J. E. Greene et al. 2026; K. Inayoshi 2025; K. Inayoshi & R. Maiolino 2025; R. P. Naidu et al. 2026).

Additionally, the relatively low SFR as well as the barely-detected host galaxies, in particular for LRDs, make their host galaxies hardly evolve to the quasar host galaxies, which are usually massive (e.g., $M_* \gtrsim 10^{10} M_\odot$ X. Ding et al. 2023, 2025; Q. Fei et al. 2026; R. Li et al. 2026; M. Onoue et al. 2025), starbursts (e.g., SFR $\sim$ 500–1000 $M_\odot\,\mathrm{yr}^{-1}$; R. Wang et al. 2013; R. Decarli et al. 2018; B. P. Venemans et al. 2020; F. Wang et al. 2024b). Indeed, their $M_*$ shows limited growth on a short timescale. This is attributable to the relatively low inferred SFRs, which is further supported by the nondetection of FIR dust emission in these targets, particularly those exhibiting red continua (H. B. Akins et al. 2025; C. M. Casey et al. 2025).

Beyond the comparison of $M_{\rm BH}$ and $M_*$, the fundamental physical distinctions between GNz7q and the LRDs can be inferred from several other aspects. First, the nature of the obscuration differs significantly. GNz7q exhibits substantial dust reddening consistent with a classic obscured quasar, while LRDs are characterized by a distinct lack of dust (e.g., R. P. Naidu et al. 2026). Second, the optical Fe II emission in GNz7q presents as a strong, broad complex, in sharp contrast to the narrow Fe II features typically observed in LRD spectra (e.g., F. D'Eugenio et al. 2025; A. Torralba et al. 2026). Finally, we find no evidence in GNz7q for the high column density of neutral gas that is always seen in LRDs (J. Matthee et al. 2024; K. Inayoshi & R. Maiolino 2025), which manifests as significant Balmer breaks or Balmer absorption lines. The absence of these features suggests that GNz7q is distinct from the LRD population. Instead, these features reinforce the scenario that GNz7q represents a progenitor to the standard population of luminous blue quasars.

Overall, the derived properties and the modeled evolutionary trajectory of GNz7q position it as a plausible direct progenitor of the luminous quasars so far discovered by ground-based facilities during a decades-long search, while the distinct evolutionary pathway of the faint JWST AGNs suggests they may constitute an intrinsically separate population in the high-redshift universe (K. Inayoshi & L. C. Ho 2025). A key question then is: How could a system like GNz7q have escaped from the "stellar-deficient" earlier stage that may be a legacy of the initial seeding process? This possible bifurcation in early growth trajectories could reflect differences in the large-scale cosmic environment, to be assessed in future work.

## 5. Conclusion

In this work, we presented a comprehensive multiwavelength characterization of GNz7q, a red quasar at $z = 7.1899$, utilizing the full suite of JWST instrumentation (NIRCam, NIRSpec, and MIRI) and archival data. This analysis provides novel insights into the rapid BH growth and the coevolutionary scenario of galaxy-BH systems in the early Universe.

Through a detailed analysis of the NIRSpec spectroscopy, we derived the following properties for the central AGN:

1. The spectrum exhibits broad Balmer emission lines (H$\alpha$, H$\beta$, H$\gamma$) and strong Fe II lines. Kinematic decomposition of the broad lines reveals a double-Gaussian profile, comprising a narrower (FWHM $\approx$ 2200 km s$^{-1}$), systemic component and a significantly broader (FWHM $\approx$ 11,000 km s$^{-1}$), highly redshifted ($\Delta v \approx$ 3600 km s$^{-1}$) component.
2. The Balmer decrement of the narrow emission lines (H$\alpha$/H$\beta$ ratio) and the continuum SED slope suggest a relatively low level of dust attenuation within the BLR. Assuming a standard extinction law, we derive an extinction of $A_V = 0.21^{+0.09}_{-0.08}$.
3. Applying local virial scaling relations yields a BH mass of $\log(M_{\rm BH}/M_\odot) = 7.55 \pm 0.34$ and a super-Eddington accretion ratio of $\lambda_{\rm Edd} = 2.7 \pm 0.4$. These properties identify GNz7q as a rapidly growing massive BH in the Epoch of Reionization, exhibiting one of the highest known accretion rates at this redshift.
4. This high Eddington accretion rate is further supported by the detection of the broad neutral [O I] emission line, which has been observed in several high-$z$ faint AGNs discovered by JWST.
5. The observed X-ray bolometric correction ($k_{\rm bol}$) presents a significant deviation ($>5\sigma$) from the empirical relations, implying a suppression of the X-ray emission in GNz7q. This depression is likely attributable to the intrinsic effects of a high accretion rate, heavy obscuration by high column density material along the line of sight, or the interplay of both mechanisms.

Utilizing NIRCam and MIRI imaging alongside MIRI spectroscopy, the host galaxy of this system is characterized as:

1. Morphological decomposition robustly resolves the host galaxy's stellar continuum in the rest-frame optical and NIR bands, revealing an effective radius of $R_e = 1.01$ kpc and a Sérsic index of $n = 1.9$. In the rest-frame MIR, the stellar contribution declines, indicating the transition to a regime dominated by thermal emission from the AGN dust torus. Interestingly, high-resolution rest-frame UV imaging reveals a clumpy morphology characterized by two distinct structures.
2. The SED fitting yields a decomposition consistent with standard system components. The rest-frame UV is driven by the AGN, while the host stellar emission becomes important in the rest-optical/NIR band. In the MIR band, the SED is dominated by the hot torus emission. The thermal emission from the dust in the host galaxy dominates the FIR and submillimeter emission.
3. The FIR SED implies a vigorous star formation rate of $\mathrm{SFR_{FIR}} = 330 \pm 97\,M_\odot\,\mathrm{yr}^{-1}$, confirming the host as a dusty starburst. This value is consistent, within uncertainties, with the independent estimate derived from the Pa$\alpha$ emission line ($\mathrm{SFR_{Pa\alpha}} = 250 \pm 88\,M_\odot\,\mathrm{yr}^{-1}$).
4. The SED fitting yields a substantial dust attenuation for the host galaxy ($A_{V,\rm host} = 3.1 \pm 0.8$). This value significantly exceeds the attenuation derived for the central AGN component, pointing to distinct dust distributions obscuring the host galaxy and the central engine, respectively.

The derived properties of the BH and host galaxy position GNz7q in a unique phase of the BH–galaxy coevolution scenario:

1. In contrast to many JWST-identified faint AGNs and high-$z$ quasars discovered from all-sky surveys that appear overmassive relative to their hosts, GNz7q exhibits a mass ratio of $M_{\rm BH}/M_* \approx 0.1\%$, placing it consistently on the local $M_{\rm BH}$–$M_*$ scaling relation. This

alignment suggests that a BH–galaxy scaling relation broadly compatible with the local one can already be observed as early as $z = 7.19$. However, we caution that the apparent overmassive nature of many JWST-identified AGNs may partly arise from an intrinsically large scatter in the $M_{\rm BH}$–$M_*$ relation combined with luminosity-driven selection biases (e.g., J. Li et al. 2025; J. Silverman et al. 2025). The location of GNz7q on the local relation is better interpreted as one representative measurement rather than definitive evidence for its universal early establishment.

2. In conclusion, GNz7q offers a rare glimpse into the progenitor phase of luminous quasars, illustrating a distinct stage of early coevolution before the onset of the unobscured, SDSS-like quasar regime.

The modeled evolutionary trajectory of GNz7q identifies it as a dust-obscured, super-Eddington progenitor likely representing an early assembly phase of luminous $z \sim 6$ quasars. Consequently, we anticipate that future deep surveys targeting higher redshifts ($z \gtrsim$ 8–10) will unveil a population of progenitor systems that have similar properties to those of GNz7q. Crucially, our growth models suggest these earlier sources will not exhibit the extreme "overmassive" BH mass ratios seen in most faint AGN populations. Instead, they should populate the extension of the local $M_{\rm BH}$–$M_*$ scaling relation. This prediction implies that the physical coupling between BH accretion and host galaxy assembly is likely established within the first few hundred million years of the Universe.

## Acknowledgments

We are grateful to Jinyi Yang and Feige Wang for their insightful discussions about the broad-line fitting. We are grateful to Zhiwei Pan and Yuming Fu for their discussions about the BH mass estimator.

K.I. acknowledges support from the National Natural Science Foundation of China (12573015, W2532003), the Beijing Natural Science Foundation (IS25003), and the China Manned Space Program (CMS-CSST-2025-A09). LCH was supported by the National Science Foundation of China (12233001) and the China Manned Space Program (CMS-CSST-2025-A09). P.G.P.-G. acknowledges support from grant PID2022-139567NB-I00 funded by the Spanish Ministerio de Ciencia, Innovación y Universidades MCIU/AEI/10.13039/501100011033, FEDER *Una manera de hacer Europa*. J.A.-M. acknowledges support by grants PID2024-158856NA-I00 & PIB2021-127718NB-I00 from the Spanish Ministry of Science and Innovation/State Agency of Research MCIN/AEI/10.13039/501100011033 and by "ERDF A way of making Europe."

This work is based on observations made with the NASA/ESA/CSA James Webb Space Telescope. The data were obtained from the Mikulski Archive for Space Telescopes at the Space Telescope Science Institute, which is operated by the Association of Universities for Research in Astronomy, Inc., under NASA contract NAS 5-03127 for JWST. The specific observations analyzed can be accessed via DOI: 10.17909/q19z-a348for the GNz7q observations and DOI: 10.17909/0akt-xx69for the MIRI images from the MEOW survey. These observations are associated with programs # 4762 and # 5407.

## Data Availability

The reduced 1D NIRSpec/G395M spectra, the MIRI LRS 1D extraction, and the MIRI MRS 1D extraction used in this work are publicly available on Zenodo at DOI: 10.5281/zenodo.21539999.

*Facilities:* JWST, IRAM:NOEMA.

*Software:* `GalfitS` (R. Li et al. 2026), `LMFIT` (M. Newville et al. 2014), `grizli` (G. Brammer & J. Matharu 2021), `msaexp` (G. Brammer 2023).

## Appendix A
## Evaluation of Additional Spectral Components

The inherent complexity and multicomponent nature of quasar spectra can make the fitting results highly dependent on the adopted model. We therefore performed a model comparison, evaluating a suite of models with different combinations of components and parameter constraints. To identify the optimal description, we employed the Bayesian information criterion (BIC):

$$\mathrm{BIC} \equiv \chi^2 + k \ln n, \tag{A1}$$

where $k$ is the number of free parameters, and $n$ is the number of data points. The model that yielded the minimum BIC value, representing the best compromise between goodness of fit ($\chi^2$) and model simplicity (penalized by $k$), was adopted as our final best fit.

We first performed a model comparison to determine the optimal number of Gaussian components required to characterize the broad Balmer lines. A simple, single-component model is strongly disfavored, yielding a 2000 km s$^{-1}$ redshift relative to the systemic velocity and a significantly poorer fit ($\Delta$BIC = 116) compared to the model in Section 3.1 (Figure A1). Conversely, models incorporating three or more components provided no statistically significant improvement. We thus conclude that our two-component model provides the most parsimonious and statistically robust description of this source's BLR. This redshifted broad H$\beta$ component has been observed in other sources at different redshifts, in particular for sources with high Eddington accretion rates (P. Marziani et al. 2009), whose origin is still under debate, while all potential explanations regard it as a nonvirial component within the BLR. Therefore, we estimate the BH and AGN properties only using the nBLR.

We also consider the possibility that the iron emission lines have the same broadening and shifting as the H$\beta$ emission line (J. W. Sulentic et al. 2012). In this consideration, we fixed the line width of the Fe II lines to that of the broad H$\beta$ component (the extremely broad component is not included). However, it failed to reproduce prominent features in the iron pseudo-continuum, particularly the emission spikes in the rest-frame 5100–5500 Å (Figure A2). More importantly, this model is disfavored by a significantly larger BIC ($\Delta$BIC = 110). Therefore, we conclude that the iron-emitting region is kinematically decoupled from the BLR in this source. Our best-fit model, which allowed the Fe II width to be a free parameter, converged on a significantly narrower profile, with $\mathrm{FWHM_{Fe}}/\mathrm{FWHM_{H\beta}} \approx 46\%$. This model comparison confirms that our fiducial setup (Section 3.1) is preferred.

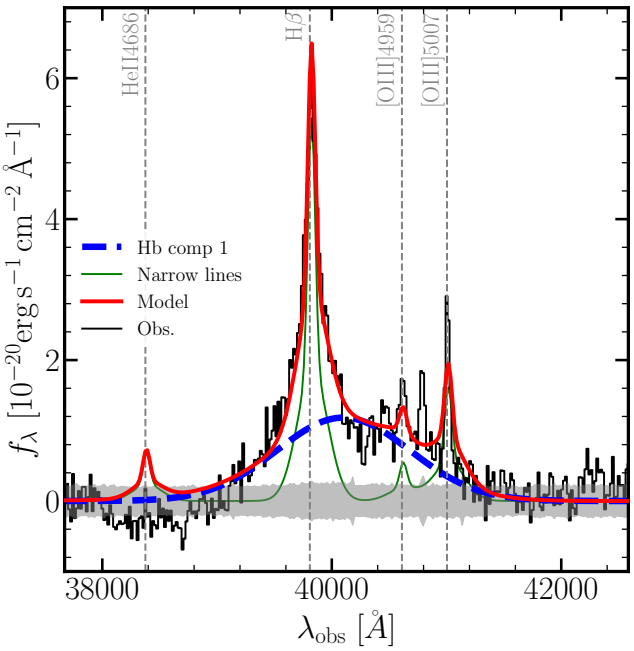



**Figure A1.** Spectral fit of the H$\beta$+[O III] complex adopting a single-component model for the broad emission line. The continuum-subtracted spectrum is shown as a black solid line, and the best-fit model is shown as a red thick line. The narrow-line model and the broad-line model are shown as a green line and a blue dashed line, respectively.

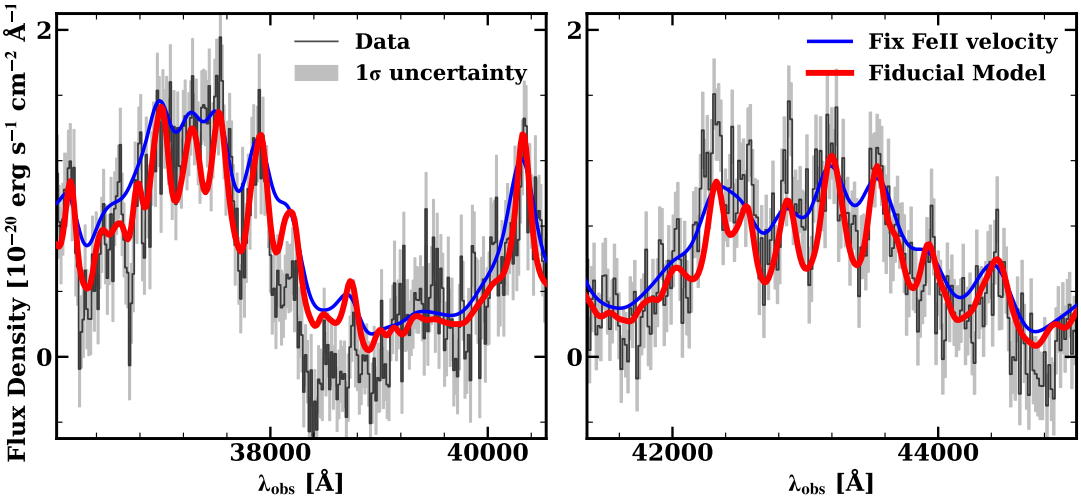



**Figure A2.** Comparison of different kinematic models for iron. The observed spectrum is shown in black for the rest-frame 4400–4950 Åand 5050–5500 Å regions. The blue line indicates the iron pseudo-continuum with the line width constrained to match the broad H$\beta$ profile, while the red line represents our fiducial model.

## Appendix B
## MIRI LRS Spectrum

Figure B1 illustrates the two-dimensional and extracted one-dimensional MIRI LRS spectra, accompanied by the best-fit model and corresponding residuals. Due to the limited spectral resolution inherent to the MIRI LRS instrument, the line widths for the NIR features were not constrained in this analysis.

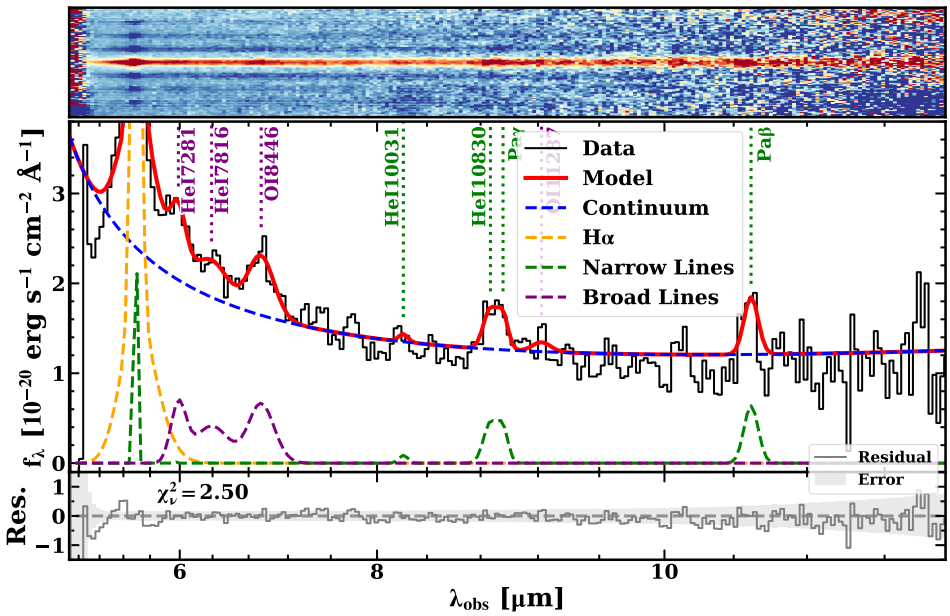



**Figure B1.** The observed rest-frame optical-to-NIR spectrum, generated from the MIRI LRS observation. Top: 2D spectrum from the MIRI LRS observation. Middle: 1D spectrum extracted from the 2D spectrum and the corresponding model. Black and red solid lines represent the observed spectrum and the resultant best-fit model, respectively. Component modeling includes a power-law continuum (blue dashed line), H$\alpha$ emission (orange dashed line), and decoupled narrow (green) and broad (purple) emission-line profiles. The corresponding emission lines are labeled with different colors (purple for broad lines and green for narrow lines). Note that we do not consider the instrumental broadening during the fitting; the broadening of those rest-frame NIR lines can be caused by the instrument. Bottom: the residual between the data and the model. The 1$\sigma$ error is shown as the gray-shaded region.

## ORCID iDs

Qinyue Fei https://orcid.org/0000-0001-7232-5355
Seiji Fujimoto https://orcid.org/0000-0001-7201-5066
Gabriel Brammer https://orcid.org/0000-0003-2680-005X
Ruancun Li https://orcid.org/0000-0001-8496-4162
Luis C. Ho https://orcid.org/0000-0001-6947-5846
Volker Bromm https://orcid.org/0000-0003-0212-2979
Javier Álvarez-Márquez https://orcid.org/0000-0002-7093-1877
Yoshihisa Asada https://orcid.org/0000-0003-3983-5438
Guillermo Barro https://orcid.org/0000-0001-6813-875X
Luis Colina https://orcid.org/0000-0002-9090-4227
Pratika Dayal https://orcid.org/0000-0001-8460-1564
Steven L. Finkelstein https://orcid.org/0000-0001-8519-1130
Johan P. U. Fynbo https://orcid.org/0000-0002-8149-8298
Michele Ginolfi https://orcid.org/0000-0002-9122-1700
Kohei Inayoshi https://orcid.org/0000-0001-9840-4959
Vasily Kokorev https://orcid.org/0000-0002-5588-9156
Gene C. K. Leung https://orcid.org/0000-0002-9393-6507
Jorryt Matthee https://orcid.org/0000-0003-2871-127X
Romain A. Meyer https://orcid.org/0000-0001-5492-4522
Rohan P. Naidu https://orcid.org/0000-0003-3997-5705
Masafusa Onoue https://orcid.org/0000-0003-2984-6803
Pablo G. Pérez-González https://orcid.org/0000-0003-4528-5639
Charles L. Steinhardt https://orcid.org/0000-0003-3780-6801
Francesco Valentino https://orcid.org/0000-0001-6477-4011
Fabian Walter https://orcid.org/0000-0003-4793-7880
Mengyuan Xiao https://orcid.org/0000-0003-1207-5344
Haowen Zhang https://orcid.org/0000-0002-4321-3538

## References

Abuter, R., Allouche, F., Amorim, A., et al. 2024, Natur, 627, 281
Akins, H. B., Casey, C. M., Lambrides, E., et al. 2025, ApJ, 991, 37
Alberts, S., Lyu, J., Shivaei, I., et al. 2024, ApJ, 976, 224
Allen, N., Oesch, P. A., Toft, S., et al. 2025, A&A, 698, A30
Álvarez-Márquez, J., Crespo Gómez, A., Colina, L., et al. 2023, A&A, 671, A105
Álvarez-Márquez, J., Colina, L., Crespo Gómez, A., et al. 2024, A&A, 686, A85
Argyriou, I., Glasse, A., Law, D. R., et al. 2023, A&A, 675, A111
Asada, Y., Inayoshi, K., Fei, Q., Fujimoto, S., & Willott, C. 2026, arXiv:2601.10573
Atek, H., Chisholm, J., Kokorev, V., et al. 2025, arXiv:2511.07542
Bañados, E., Venemans, B. P., Mazzucchelli, C., et al. 2018, Natur, 553, 473
Bean, R., & Magueijo, J. 2002, PhRvD, 66, 063505
Bezanson, R., Labbe, I., Whitaker, K. E., et al. 2024, ApJ, 974, 92
Bik, A., Álvarez-Márquez, J., Colina, L., et al. 2024, A&A, 686, A3
Boquien, M., Burgarella, D., Roehlly, Y., et al. 2019, A&A, 622, A103
Boroson, T. A., & Green, R. F. 1992, ApJS, 80, 109
Bosman, S. E. I., Álvarez-Márquez, J., Colina, L., et al. 2024, NatAs, 8, 1054
Bosman, S. E. I., Álvarez-Márquez, J., Davies, F. B., et al. 2025, arXiv:2511.02902
Brammer, G. 2023, msaexp: NIRSpec analysis tools, v0.6.17, Zenodo, doi:10.5281/zenodo.7299500
Brammer, G., & Matharu, J. 2021, gbrammer/grizli: v1.3.2, Zenodo, doi:10.5281/zenodo.5012699
Brammer, G., Strait, V., Matharu, J., & Momcheva, I. 2022, grizli, v1.5.0, Zenodo, doi:10.5281/zenodo.6672538
Bruzual, G., & Charlot, S. 2003, MNRAS, 344, 1000
Bushouse, H., Eisenhamer, J., Dencheva, N., et al. 2024, JWST Calibration Pipeline, v1.14.0, Zenodo, doi:10.5281/zenodo.10870758
Calzetti, D. 2001, PASP, 113, 1449
Calzetti, D., Armus, L., Bohlin, R. C., et al. 2000, ApJ, 533, 682
Carr, B., & Kühnel, F. 2020, ARNPS, 70, 355
Casey, C. M., Akins, H. B., Finkelstein, S. L., et al. 2025, ApJL, 990, L61
Chabrier, G. 2003, PASP, 115, 763
Chang, S.-J., Gronke, M., Matthee, J., & Mason, C. 2025, MNRAS, 545, staf2131
Chen, C.-H., Ho, L. C., Li, R., & Inayoshi, K. 2025a, ApJL, 989, L12
Chen, C.-H., Ho, L. C., Li, R., & Zhuang, M.-Y. 2025b, ApJ, 983, 60
Czerny, B., Wang, J.-M., Du, P., et al. 2019, ApJ, 870, 84
Dayal, P. 2024, A&A, 690, A182
Dayal, P., Rossi, E. M., Shiralilou, B., et al. 2019, MNRAS, 486, 2336
de Graaff, A., Setton, D. J., Brammer, G., et al. 2025a, NatAs, 9, 280
de Graaff, A., Brammer, G., Weibel, A., et al. 2025b, A&A, 697, A189
Decarli, R., Walter, F., Venemans, B. P., et al. 2018, ApJ, 854, 97

D'Eugenio, F., Nelson, E., Ji, X., et al. 2025, arXiv:2510.00101
Di Mascia, F., Gallerani, S., Ferrara, A., et al. 2021, MNRAS, 506, 3946
Ding, X., Onoue, M., Silverman, J. D., et al. 2023, Natur, 621, 51
Ding, X., Onoue, M., Silverman, J. D., et al. 2025, ApJ, 993, 91
Domínguez, A., Siana, B., Henry, A. L., et al. 2013, ApJ, 763, 145
Dong, X., Wang, T., Wang, J., et al. 2008, MNRAS, 383, 581
Donley, J. L., Koekemoer, A. M., Brusa, M., et al. 2012, ApJ, 748, 142
Du, P., & Wang, J.-M. 2019, ApJ, 886, 42
Du, P., Hu, C., Lu, K.-X., et al. 2015, ApJ, 806, 22
Du, P., Lu, K.-X., Zhang, Z.-X., et al. 2016, ApJ, 825, 126
Du, P., Zhang, Z.-X., Wang, K., et al. 2018, ApJ, 856, 6
Dunlop, J. S., Abraham, R. G., Ashby, M. L. N., et al. 2021, PRIMER: Public Release IMaging for Extragalactic Research Cycle 1, ID. #1837, JWST Proposal
Duras, F., Bongiorno, A., Ricci, F., et al. 2020, A&A, 636, A73
Eisenstein, D. J., Johnson, B. D., Robertson, B., et al. 2025, ApJS, 281, 50
Fan, X., Bañados, E., & Simcoe, R. A. 2023, ARA&A, 61, 373
Fan, X., Narayanan, V. K., Lupton, R. H., et al. 2001, AJ, 122, 2833
Fan, X., Strauss, M. A., Richards, G. T., et al. 2006, AJ, 131, 1203
Farina, E. P., Schindler, J.-T., Walter, F., et al. 2022, ApJ, 941, 106
Fei, Q., Fujimoto, S., Naidu, R. P., et al. 2026, ApJ, 1003, 244
Fei, Q., Silverman, J. D., Fujimoto, S., et al. 2025, ApJ, 980, 84
Ferrarese, L., & Merritt, D. 2000, ApJL, 539, L9
Fu, S., Zhang, Z., Jiang, D., et al. 2026, NatAs, Advanced Online Publication
Fujimoto, S., Brammer, G. B., Watson, D., et al. 2022, Natur, 604, 261
Furtak, L. J., Labbé, I., Zitrin, A., et al. 2024, Natur, 628, 57
Gallerani, S., Maiolino, R., Juarez, Y., et al. 2010, A&A, 523, A85
Gebhardt, K., Bender, R., Bower, G., et al. 2000, ApJL, 539, L13
Gillman, S., Smail, I., Gullberg, B., et al. 2024, A&A, 691, A299
Gordon, K. D., Clayton, G. C., Misselt, K. A., Landolt, A. U., & Wolff, M. J. 2003, ApJ, 594, 279
Greene, J. E., & Ho, L. C. 2005, ApJ, 630, 122
Greene, J. E., Strader, J., & Ho, L. C. 2020, ARA&A, 58, 257
Greene, J. E., Labbe, I., Goulding, A. D., et al. 2024, ApJ, 964, 39
Greene, J. E., Setton, D. J., Furtak, L. J., et al. 2026, ApJ, 996, 129
Guo, H., Shen, Y., & Wang, S. 2018, PyQSOFit: Python code to fit the spectrum of quasars, Astrophysics Source Code Library,, ascl: 1809.008
Harikane, Y., Zhang, Y., Nakajima, K., et al. 2023, ApJ, 959, 39
Heintz, K. E., Brammer, G. B., Watson, D., et al. 2025, A&A, 693, A60
Hopkins, P. F., Hernquist, L., Cox, T. J., & Kereš, D. 2008, ApJS, 175, 356
Horne, K. 1986, PASP, 98, 609
Hviding, R. E., de Graaff, A., Miller, T. B., et al. 2025, A&A, 702, A57
Ilić, D., Oknyansky, V., Popović, L. Č., et al. 2020, A&A, 638, A13
Inayoshi, K. 2025, ApJL, 988, L22
Inayoshi, K., & Ho, L. C. 2025, arXiv:2512.03130
Inayoshi, K., Kimura, S. S., & Noda, H. 2025, PASJ, 77, 811
Inayoshi, K., & Maiolino, R. 2025, ApJL, 980, L27
Inayoshi, K., Onoue, M., Sugahara, Y., Inoue, A. K., & Ho, L. C. 2022, ApJL, 931, L25
Inayoshi, K., Visbal, E., & Haiman, Z. 2020, ARA&A, 58, 27
Izumi, T., Onoue, M., Matsuoka, Y., et al. 2019, PASJ, 71, 111
Jeon, J., Bromm, V., Liu, B., & Finkelstein, S. L. 2025, ApJ, 979, 127
Jeon, J., Liu, B., Bromm, V., et al. 2026, ApJ, 998, 148
Jiang, F., Jia, Z., Zheng, H., et al. 2026, ApJL, 996, L19
Jones, O. C., Álvarez-Márquez, J., Sloan, G. C., et al. 2023, MNRAS, 523, 2519
Juodžbalis, I., Marconcini, C., D'Eugenio, F., et al. 2026, Natur, 653, 1017
Kaspi, S., Smith, P. S., Netzer, H., et al. 2000, ApJ, 533, 631
Kato, N., Matsuoka, Y., Onoue, M., et al. 2020, PASJ, 72, 84
Kendrew, S., Scheithauer, S., Bouchet, P., et al. 2015, PASP, 127, 623
King, A. 2024, MNRAS, 531, 550
Kocevski, D. D., Onoue, M., Inayoshi, K., et al. 2023, ApJL, 954, L4
Kokorev, V., Fujimoto, S., Labbe, I., et al. 2023, ApJL, 957, L7
Kokorev, V., Chisholm, J., Naidu, R. P., et al. 2026, ApJ, 1004, 153
Kormendy, J., & Ho, L. C. 2013, ARA&A, 51, 511
Kroupa, P. 2001, MNRAS, 322, 231
Labiano, A., Argyriou, I., Álvarez-Márquez, J., et al. 2021, A&A, 656, A57
Larson, R. L., Finkelstein, S. L., Kocevski, D. D., et al. 2023, ApJL, 953, L29
Law, D. R., E. Morrison, J., Argyriou, I., et al. 2023, AJ, 166, 45
Leung, G. C. K., Endsley, R., Finkelstein, S. L., et al. 2024, MEOW: The MIRI Early Obscured-AGN Wide Survey Cycle 3, ID. #5407, JWST Proposal
Li, J., Silverman, J. D., Ding, X., et al. 2021, ApJ, 922, 142
Li, J., Silverman, J. D., Shen, Y., et al. 2025, ApJ, 981, 19
Li, R., Ho, L. C., & Chen, C.-H. 2026, ApJ, 999, 70
Li, R., Ho, L. C., Ricci, C., et al. 2022, ApJ, 933, 70
Li, W., Inayoshi, K., Onoue, M., et al. 2024, ApJ, 969, 69
Lin, X., Wang, F., Fan, X., et al. 2024, ApJ, 974, 147
Lin, X., Fan, X., Wang, F., et al. 2026, ApJ, 996, 93
Lupi, A., Trinca, A., Volonteri, M., Dotti, M., & Mazzucchelli, C. 2024, A&A, 689, A128
Lusso, E., Comastri, A., Vignali, C., et al. 2010, A&A, 512, A34
Madau, P., & Dickinson, M. 2014, ARA&A, 52, 415
Madau, P., & Haardt, F. 2024, ApJL, 976, L24
Magorrian, J., Tremaine, S., Richstone, D., et al. 1998, AJ, 115, 2285
Maheson, G., Maiolino, R., Curti, M., et al. 2024, MNRAS, 527, 8213
Maiolino, R., Schneider, R., Oliva, E., et al. 2004, Natur, 431, 533
Maiolino, R., Scholtz, J., Witstok, J., et al. 2024a, Natur, 627, 59
Maiolino, R., Scholtz, J., Curtis-Lake, E., et al. 2024b, A&A, 691, A145
Maiolino, R., Risaliti, G., Signorini, M., et al. 2025, MNRAS, 538, 1921
Maithil, J., Brotherton, M. S., Shemmer, O., et al. 2022, MNRAS, 515, 491
Marshall, M. A., Mechtley, M., Windhorst, R. A., et al. 2020, ApJ, 900, 21
Marziani, P., Sulentic, J. W., Stirpe, G. M., Zamfir, S., & Calvani, M. 2009, A&A, 495, 83
Matsuoka, Y., Strauss, M. A., Kashikawa, N., et al. 2018, ApJ, 869, 150
Matthee, J., Naidu, R. P., Brammer, G., et al. 2024, ApJ, 963, 129
Mechtley, M., Windhorst, R. A., Ryan, R. E., et al. 2012, ApJL, 756, L38
Momcheva, I. G., Lee, J. C., Ly, C., et al. 2013, AJ, 145, 47
Mortlock, D. J., Warren, S. J., Venemans, B. P., et al. 2011, Natur, 474, 616
Naidu, R. P., Matthee, J., Katz, H., et al. 2026, Natur, 656, 329
Nakajima, K., Ouchi, M., Isobe, Y., et al. 2023, ApJS, 269, 33
Neeleman, M., Novak, M., Venemans, B. P., et al. 2021, ApJ, 911, 141
Newville, M., Stensitzki, T., Allen, D. B., & Ingargiola, A. 2014, LMFIT: Non-Linear Least-Square Minimization and Curve-Fitting for Python, 0.8.0, Zenodo, doi:10.5281/zenodo.11813
Oesch, P. A., Brammer, G., Naidu, R. P., et al. 2023, MNRAS, 525, 2864
Oke, J. B., & Gunn, J. E. 1983, ApJ, 266, 713
Onoue, M., Ding, X., Silverman, J. D., et al. 2025, NatAs, 9, 1541
Osterbrock, D. E. 1989, Astrophysics of Gaseous Nebulae and Active Galactic Nuclei (University Science Books)
Östlin, G., Pérez-González, P. G., Melinder, J., et al. 2025, A&A, 696, A57
Pacucci, F., & Loeb, A. 2024, ApJ, 964, 154
Pacucci, F., Nguyen, B., Carniani, S., Maiolino, R., & Fan, X. 2023, ApJL, 957, L3
Pan, Z., Jiang, L., Guo, W.-J., et al. 2025, ApJ, 987, 48
Pérez-González, P. G., Barro, G., Rieke, G. H., et al. 2024, ApJ, 968, 4
Price, S. H., Bezanson, R., Labbe, I., et al. 2025, ApJ, 982, 51
Reddy, N. A., Topping, M. W., Sanders, R. L., Shapley, A. E., & Brammer, G. 2023, ApJ, 948, 83
Reed, S. L., Banerji, M., Becker, G. D., et al. 2019, MNRAS, 487, 1874
Reines, A. E., & Volonteri, M. 2015, ApJ, 813, 82
Ren, W., Guo, H., Shen, Y., et al. 2024, ApJ, 974, 153
Rieke, G. H., Wright, G. S., Böker, T., et al. 2015, PASP, 127, 584
Rieke, M. J., Robertson, B., Tacchella, S., et al. 2023, ApJS, 269, 16
Rusakov, V., Watson, D., Nikopoulos, G. P., et al. 2026, Natur, 8097, 574
Sanders, D. B., Soifer, B. T., Elias, J. H., Neugebauer, G., & Matthews, K. 1988, ApJL, 328, L35
Sanders, R. L., Shapley, A. E., Topping, M. W., et al. 2025, ApJ, 989, 209
Selsing, J., Fynbo, J. P. U., Christensen, L., & Krogager, J.-K. 2016, A&A, 585, A87
Shen, Y., Greene, J. E., Ho, L. C., et al. 2015, ApJ, 805, 96
Shen, Y., Wu, J., Jiang, L., et al. 2019, ApJ, 873, 35
Shen, Y., Grier, C. J., Horne, K., et al. 2024, ApJS, 272, 26
Silverman, J., Li, J., Ding, X., et al. 2025, ApJL, 995, L67
Skilling, J. 2004, AIPC, 735, 395
Sloan, G., Murray, K., Noriega-Crespo, A., & Petric, A. 2024, JWST Proposal. Cycle 3, ID. #6620
Smith, A., & Bromm, V. 2019, ConPh, 60, 111
Son, S., Kim, M., Ho, L. C., & Li, R. 2025, ApJ, 995, 37
Stalevski, M., Ricci, C., Ueda, Y., et al. 2016, MNRAS, 458, 2288
Stone, M. A., Lyu, J., Rieke, G. H., Alberts, S., & Hainline, K. N. 2024, ApJ, 964, 90
Storey, P. J., & Zeippen, C. J. 2000, MNRAS, 312, 813
Sulentic, J. W., Marziani, P., Zamanov, R., et al. 2002, ApJL, 566, L71
Sulentic, J. W., Marziani, P., Zamfir, S., & Meadows, Z. A. 2012, ApJL, 752, L7
Sun, W. Q., Naidu, R. P., Matthee, J., et al. 2026, OJAp, 9, 62505
Tadaki, K., Iono, D., Yun, M. S., et al. 2018, Natur, 560, 613
Tanaka, T. S., Silverman, J. D., Ding, X., et al. 2025, ApJ, 979, 215
Taylor, A. J., Finkelstein, S. L., Kocevski, D. D., et al. 2025a, ApJ, 986, 165
Taylor, A. J., Kokorev, V., Kocevski, D. D., et al. 2025b, ApJL, 989, L7
Torralba, A., Matthee, J., Pezzulli, G., et al. 2026, A&A, 707, A75

Trakhtenbrot, B., Netzer, H., Lira, P., & Shemmer, O. 2011, ApJ, 730, 7
Trinca, A., Lupi, A., Haardt, F., & Madau, P. 2026a, A&A, 710, A289
Trinca, A., Valiante, R., Schneider, R., et al. 2026b, MNRAS, stag1608, Advance Access
Tripodi, R., Martis, N., Markov, V., et al. 2025, NatCo, 16, 9830
Tripodi, R., Bradač, M., D'Eugenio, F., et al. 2025, ApJL, 994, L6
Umeda, H., Inayoshi, K., Harikane, Y., & Murase, K. 2026, ApJ, 999, 183
Valentino, F., Brammer, G., Gould, K. M. L., et al. 2023, ApJ, 947, 20
Valentino, F., Heintz, K. E., Brammer, G., et al. 2025, A&A, 699, A358
Venemans, B. P., Walter, F., Neeleman, M., et al. 2020, ApJ, 904, 130
Vestergaard, M., & Peterson, B. M. 2006, ApJ, 641, 689
Volonteri, M. 2012, Sci, 337, 544
Walter, F., Carilli, C., Bertoldi, F., et al. 2004, ApJL, 615, L17
Wang, B., Leja, J., de Graaff, A., et al. 2024a, ApJL, 969, L13
Wang, B., de Graaff, A., Davies, R. L., et al. 2025, ApJ, 984, 121
Wang, F., Yang, J., Fan, X., et al. 2021a, ApJL, 907, L1
Wang, F., Fan, X., Yang, J., et al. 2021b, ApJ, 908, 53
Wang, F., Yang, J., Fan, X., et al. 2024b, ApJ, 968, 9
Wang, J.-M., Qiu, J., Du, P., & Ho, L. C. 2014, ApJ, 797, 65
Wang, R., Carilli, C. L., Neri, R., et al. 2010, ApJ, 714, 699
Wang, R., Wagg, J., Carilli, C. L., et al. 2013, ApJ, 773, 44
Wells, M., Pel, J.-W., Glasse, A., et al. 2015, PASP, 127, 646
Woods, T. E., Agarwal, B., Bromm, V., et al. 2019, PASA, 36, e027
Wright, G. S., Wright, D., Goodson, G. B., et al. 2015, PASP, 127, 595
Wright, G. S., Rieke, G. H., Glasse, A., et al. 2023, PASP, 135, 048003
Wright, L., Whitaker, K. E., Weaver, J. R., et al. 2024, ApJL, 964, L10
Yan, Z., Inayoshi, K., Chen, K., & Guo, J. 2026, ApJ, 1002, 159
Yang, G., Boquien, M., Brandt, W. N., et al. 2022, ApJ, 927, 192
Yang, J., Wang, F., Fan, X., et al. 2021, ApJ, 923, 262
Yang, J., Wang, F., Fan, X., et al. 2023, ApJL, 951, L5
Yue, M., Eilers, A.-C., Simcoe, R. A., et al. 2024, ApJ, 966, 176
Zhang, S., Liu, B., Bromm, V., et al. 2025, ApJ, 987, 185
Zhuang, M.-Y., & Ho, L. C. 2023, NatAs, 7, 1376